



NAVAL POSTGRADUATE SCHOOL

MONTEREY, CALIFORNIA

THESIS

**CHARACTERIZATION OF 3 – 5 MICRON THERMAL
IMAGERS AND ANALYSIS OF NARROW BAND IMAGES**

by

Quek, Yew Sing

December 2004

Thesis Advisor:
Second Reader:

Alfred W. Cooper
Gamani Karunasiri

Approved for public release; distribution is unlimited.

THIS PAGE INTENTIONALLY LEFT BLANK

REPORT DOCUMENTATION PAGE			Form Approved OMB No. 0704-0188	
Public reporting burden for this collection of information is estimated to average 1 hour per response, including the time for reviewing instruction, searching existing data sources, gathering and maintaining the data needed, and completing and reviewing the collection of information. Send comments regarding this burden estimate or any other aspect of this collection of information, including suggestions for reducing this burden, to Washington headquarters Services, Directorate for Information Operations and Reports, 1215 Jefferson Davis Highway, Suite 1204, Arlington, VA 22202-4302, and to the Office of Management and Budget, Paperwork Reduction Project (0704-0188) Washington DC 20503.				
1. AGENCY USE ONLY (Leave blank)		2. REPORT DATE December 2004		3. REPORT TYPE AND DATES COVERED Master's Thesis
4. TITLE AND SUBTITLE: Characterization of 3 to 5 Micron Thermal Imagers and Analysis of Narrow Band Images			5. FUNDING NUMBERS	
6. AUTHOR(S) Quek, Yew Sing				
7. PERFORMING ORGANIZATION NAME(S) AND ADDRESS(ES) Naval Postgraduate School Monterey, CA 93943-5000			8. PERFORMING ORGANIZATION REPORT NUMBER	
9. SPONSORING /MONITORING AGENCY NAME(S) AND ADDRESS(ES) National University of Singapore and Naval Postgraduate School			10. SPONSORING/MONITORING AGENCY REPORT NUMBER TDSI / 02-005 / 1C	
11. SUPPLEMENTARY NOTES The views expressed in this thesis are those of the author and do not reflect the official policy or position of the Department of Defense or the U.S. Government.				
12a. DISTRIBUTION / AVAILABILITY STATEMENT Approved for public release; distribution is unlimited			12b. DISTRIBUTION CODE A	
13. ABSTRACT (maximum 200 words) In this study, the use of multi narrow-band filters was explored to correlate or fuse information to improve detection and recognition for specific targets of interest. To fully understand the viability and limitations of narrow band filters in thermal imaging, laboratory test procedures were first designed to characterize thermal images using common performance parameters, particularly the Noise Equivalent Temperature Difference (NETD), the Modulation Transfer Function (MTF) and the Minimum Resolvable Temperature (MRT). An available thermal imager, the Cincinnati Electronics IRRIS-256LN, and a newly purchased thermal imager, the Indigo Systems Merlin InSb Laboratory Camera, were investigated and compared. The MRT measurement showed a superior cut-off spatial frequency of 1.33 cycle/mrad for the Merlin camera, compared with 1.18 cycle/mrad for the Cincinnati, with similar sensitivity of about 0.1 °C for both cameras. Below cut-off the Modulation Transfer for the Merlin was approximately twice that of the Cincinnati. NETD measurements for both systems were inhibited by excess noise in the measurement system. The Merlin camera was consequently employed for further research on narrow band images. Three commercially available narrow band filters, 4110/4720 nm, 4540/4720 nm and 3750/4020 nm, were selected to isolate the "red" and "blue" spike signatures of plume emission and aerodynamic heating found in the signature of fast moving air targets. Similar sensor characterization was carried out with these filters, however, quantitative performance parameter measurements were hindered by excessive measurement system noise. As a preliminary study in multi-spectral image analysis, spectral features of hydrocarbon combustion were extracted from correlated narrow-band images of a laboratory propane flame. Digital analysis using software statistical tools showed potential for discrimination of hydrocarbon emission from other thermal sources by correlating pixel number and pixel radiant intensity.				
14. SUBJECT TERMS Thermal Imager, narrow band images, narrow band filter, minimum resolvable temperature, noise equivalent temperature difference, modulation transfer function			15. NUMBER OF PAGES 109	
			16. PRICE CODE	
17. SECURITY CLASSIFICATION OF REPORT Unclassified	18. SECURITY CLASSIFICATION OF THIS PAGE Unclassified	19. SECURITY CLASSIFICATION OF ABSTRACT Unclassified	20. LIMITATION OF ABSTRACT UL	

NSN 7540-01-280-5500

Standard Form 298 (Rev. 2-89)
Prescribed by ANSI Std. Z39-18

THIS PAGE INTENTIONALLY LEFT BLANK

Approved for public release; distribution is unlimited.

**CHARACTERIZATION OF 3 – 5 MICRON THERMAL IMAGERS AND
ANALYSIS OF NARROW BAND IMAGES**

Yew Sing Quek
Captain, Singapore Armed Forces
B.Eng (Hons), Nanyang Technological University, Singapore, 1999

Submitted in partial fulfillment of the
requirements for the degree of

MASTER OF SCIENCE IN COMBAT SYSTEMS TECHNOLOGY

from the

**NAVAL POSTGRADUATE SCHOOL
December 2004**

Author: Yew Sing Quek

Approved by: Alfred W. Cooper
Thesis Advisor

Gamani Karunasiri
Thesis Co-Advisor

James Luscombe
Chairman, Department of Physics

THIS PAGE INTENTIONALLY LEFT BLANK

ABSTRACT

In this study, the use of multi narrow-band filters was explored to correlate or fuse information to improve detection and recognition for specific targets of interest. To fully understand the viability and limitations of narrow band filters in thermal imaging, laboratory test procedures were first designed to characterize thermal images using common performance parameters, particularly the Noise Equivalent Temperature Difference (NETD), the Modulation Transfer Function (MTF) and the Minimum Resolvable Temperature (MRT). An available thermal imager, the Cincinnati Electronics IRRIS-256LN, and a newly purchased thermal imager, the Indigo Systems Merlin InSb Laboratory Camera, were investigated and compared. The MRT measurement showed a superior cut-off spatial frequency of 1.33 cycle/mrad for the Merlin camera, compared with 1.18 cycle/mrad for the Cincinnati, with similar sensitivity of about 0.1 °C for both cameras. Below cut-off the Modulation Transfer for the Merlin was approximately twice that of the Cincinnati. NETD measurements for both systems were inhibited by excess noise in the measurement system. The Merlin camera was consequently employed for further research on narrow band images. Three commercially available narrow band filters, 4110/4720 nm, 4540/4720 nm and 3750/4020 nm, were selected to isolate the "red" and "blue" spike signatures of plume emission and aerodynamic heating found in the signature of fast moving air targets. Similar sensor characterization was carried out with these filters; however, quantitative performance parameter measurements were hindered by excessive measurement system noise. As a preliminary study in multi-spectral

image analysis, spectral features of hydrocarbon combustion were extracted from correlated narrow-band images of a laboratory propane flame. Digital analysis using software statistical tools showed potential for discrimination of hydrocarbon emission from other thermal sources by correlating pixel number and pixel radiant intensity.

TABLE OF CONTENTS

I.	INTRODUCTION.....	1
A.	GENERAL.....	1
B.	SCOPE OF STUDY.....	2
C.	PREVIOUS WORK DONE	2
II.	FUNDAMENTALS	5
A.	ELECTROMAGNETIC SPECTRUM	5
B.	LAWS OF THERMAL RADIATION.....	7
1.	Planck's Blackbody Radiation Law.....	7
2.	Wien's Displacement Law.....	8
C.	TARGET TO BACKGROUND CONTRAST.....	10
D.	SENSITIVITY AND RESOLUTION LIMITS.....	11
III.	PERFORMANCE PARAMETERS OF INFRARED IMAGING SYSTEMS....	15
A.	SIGNAL TRANSFER FUNCTION (SITF) AND NOISE EQUIVALENT TEMPERATURE DIFFERENCE (NETD)	15
B.	CONTRAST TRANSFER FUNCTION (CTF) AND MODULATION TRANSFER FUNCTION (MTF).....	17
C.	MINIMUM RESOLVABLE TEMPERATURE (MRT) DIFFERENCE...	20
IV.	CHARACTERIZATION OF THERMAL IMAGERS	23
A.	SYSTEM SPECIFICATIONS.....	23
1.	Cincinnati Electronics IRRIS-256LN.....	23
2.	Merlin InSb Laboratory Camera.....	24
B.	LABORATORY SET UP AND EXPERIMENTAL PROCEDURES	25
1.	Signal Transfer Function and Noise Equivalent Temperature.....	27
2.	Contrast Transfer Function and Modulation Transfer Function.....	28
3.	Minimum Resolvable Temperature Difference	29
C.	EXPERIMENTAL RESULTS AND ANALYSIS.....	30
1.	Signal Transfer Function and Noise Equivalent Temperature.....	30
2.	Contrast Transfer Function and Modulation Transfer Function.....	35
3.	Minimum Resolvable Temperature Difference	40
V.	SELECTION OF NARROW BAND FILTERS	47
A.	SPECTRAL BAND SELECTION	47
B.	EXHAUST PLUME SIGNATURE.....	48
C.	AERODYNAMIC HEATING	51
D.	NARROW BAND FILTER SELECTION.....	53
VI.	EXPERIMENTATION WITH NARROW BAND FILTERS	57
A.	CONTRAST TRANSFER FUNCTION.....	58
B.	MINIMUM RESOLVABLE TEMPERATURE DIFFERENCE	62

C.	ANALYSIS OF NARROW BAND IMAGES	65
1.	Experimental Procedures.....	65
2.	Image Intensity Windowing Statistical Analysis	68
3.	Image Area Statistical Analysis.....	74
VII.	CONCLUSIONS.....	77
VIII.	RECOMMENDATIONS FOR FUTURE WORK	79
	APPENDIX A.....	81
	APPENDIX B.....	83
	APPENDIX C.....	87
	LIST OF REFERENCES.....	91
	INITIAL DISTRIBUTION LIST	93

LIST OF FIGURES

Figure 2.1.	Electromagnetic Spectrum.	6
Figure 2.2	Planck's law plotted graphically.	8
Figure 2.3	MRT is bounded by the system's resolution and by visual sensitivity limit.	13
Figure 2.4	Two systems with different MRTs.	13
Figure 3.1	Typical responsivity function illustrating the SiTF.	16
Figure 3.2	Definition of modulation (From [2])	18
Figure 3.3	Definition of modulation transfer for three spatial frequencies: (a) input (object) modulation, (b) output (image) modulation, and (c) the MTF.	19
Figure 3.4	Relationships between CTF and MTF.	19
Figure 3.5	MRT as a function of spatial frequency.	21
Figure 4.1	The Cincinnati Electronics IRRIS-256LN.	23
Figure 4.2	The Merlin InSb Laboratory Camera.	24
Figure 4.3.	Equipment setup schematic.	25
Figure 4.4	Actual experimental setup.	26
Figure 4.5	Measured Responsivity curve for Cincinnati thermal imager.	32
Figure 4.6	Measured Responsivity curve for Merlin thermal imager.	34
Figure 4.7	Plot of CTF result for Cincinnati thermal imager.	36
Figure 4.8	CTF and MTF plots for Cincinnati Thermal Imager.	37
Figure 4.9	Plot of CTF result for Merlin thermal imager.	38
Figure 4.10	CTF and MTF plots for Merlin Thermal Imager.	39
Figure 4.11	Comparison of CTF between Merlin and Cincinnati thermal imager. .	39
Figure 4.12	MRT plot for Cincinnati thermal imager.	41
Figure 4.13	MRT plot for Merlin thermal imager.	43
Figure 4.14	Comparison of MRT between Merlin and Cincinnati thermal imager..	43
Figure 4.15	Comparison of calculated and experimental MRT.	46
Figure 5.1	Superposition of an illustrative plume emission against the atmospheric transmission.	49
Figure 5.2	Formation of the blue and red spike in an aircraft exhaust plume signature as a result of atmospheric attenuation.	50
Figure 5.3	Relative spectrum of target exhaust plume emission when viewed away from the tail aspect. (From [17]).	51
Figure 6.1	CTF of all the various filter bands	61
Figure 6.2	MRT of all the various filter bands	64
Figure 6.3	Visual image of scene to be acquired by the thermal imager.	66
Figure 6.4	Infrared emission from a Bunsen flame burning natural gas.	67
Figure 6.5	Exhaust plume radiance as a function of wavelength for five solid propellant engines. From [21].	67
Figure 6.6	Images of the propane flame acquired using IRvista interface for 3000/5000 nm and 4110/4720 nm filter bands and the corresponding image intensity histograms.	69

Figure 6.7	Images of the propane flame acquired using IRvista interface for 3750/4020 nm and 4540/4720 nm filter bands and the corresponding image intensity histograms.	70
Figure 6.8	In graphical form, the number of pixels corresponding to various peak pixel values from Figure 6.6 and 6.7. (a) Raw data (b) Normalized against background pixel number.....	73
Figure 6.9	Image area statistics using the elliptical ROI.....	75

LIST OF TABLES

Table 2.1	Definition of Radiometric Quantities.	7
Table 4.1	SiTF experimental results for Cincinnati thermal imager.	32
Table 4.2	SiTF experimental results for Merlin thermal imager.	33
Table 4.3	CTF for Cincinnati thermal imager.	35
Table 4.4	CTF for Merlin thermal imager.	38
Table 4.5	MRT for Cincinnati thermal imager.	41
Table 4.6	MRT for Merlin thermal imager.	42
Table 4.7	Parameters used for theoretical MRT calculation (Equation 3.5)	45
Table 5.1	Narrow filter bands used in this study.	54
Table 6.1	Details of calibrated Merlin Camera with narrow band filters.	58
Table 6.2	CTF values for filter band 4110/4720 nm	59
Table 6.3	CTF values for filter band 3750/4020 nm	59
Table 6.4	CTF values for filter band 4540/4720 nm	60
Table 6.5	Curve fitting parameter x for CTF of various color filters as defined in equation (4.1).	60
Table 6.6	MRT values for filter band 4110/4720 nm.	63
Table 6.7	MRT values for filter band 3750/4020 nm.	63
Table 6.8	MRT values for filter band 4540/4720 nm.	63
Table 6.9	Curve fitting parameters A, B and C of MRT for various band filters as defined in equation (4.4)	64
Table 6.10	The number of pixels corresponding to various peak pixel values from Figure 6.6 and 6.7. (a) Raw data (b) Normalized against background pixel number	72

THIS PAGE INTENTIONALLY LEFT BLANK

ACKNOWLEDGMENTS

I wish to show my appreciation to all those who have assisted and contributed one way or another to the success of this thesis.

Firstly, I will like to thank my organization, the Singapore Armed Forces, for giving me this opportunity to pursue my Masters degree in Naval Postgraduate School. Secondly, thanks to the Temasek Defense Systems Institute (TDSI), National University of Singapore, and Naval Postgraduate School for giving me the privilege to be part of this joint project. This work was supported by the TDSI under contract document number: TDSI / 02-005 / 1C. To my thesis advisor, Professor Alfred W. Cooper, thanks him for giving me the opportunity to be his student and providing me with his expert guidance. I have learnt lessons far more than just the academic aspect from him with his shared experiences. I will also like to show my gratitude to Professor Gamani Karunasiri for his guidance and help as my second reader. To the supporting staff, special thanks to Mr. Sam Barone for his constant support and assistance in the laboratory. He is always there to assist when needed in logistic matters and hands-on applications. I will also like to acknowledge the extended services provided by Dr. Austin Richards of Indigo Systems Corporation in the troubleshooting of the Merlin camera and IRvista software.

Finally, I wish to express my utmost gratitude to my wife, Bee Leng, for her understanding, constant support and sacrifices made throughout my course of work.

THIS PAGE INTENTIONALLY LEFT BLANK

I. INTRODUCTION

A. GENERAL

The invention of the infrared imager has changed the way military used to operate. For centuries, military had exploited night or low-light condition as concealment for military operations. This tactic is now obsolete with the use of the infrared devices. More importantly, modern warfare is now fought with increasing tempo and round the clock. These systems are, hence, indispensable to military forces fighting modern warfare.

The thermal imager (TI) senses any object as long as the object has temperature greater than zero Kelvin. This means that essentially all objects can be sensed using the imager. The main consideration is that to be detected, and subsequently recognized and identified, an object must produce an object-to-background apparent temperature difference of sufficient magnitude to distinguish it from other variations in the background [1]. The other advantage of a thermal imager is that it is a passive system. It can be employed without the target knowing of its presence. Because of its capabilities, the thermal sensor is now widely used for weapon targeting and surveillance. In the analysis of TI, just like many other sensor systems, attempts have been made to improve sensing range, target discrimination and false alarm rate. All these desirable quantities depend largely on system resolution and sensitivity, as well as on the operating medium.

This research task was part of an initiative between the National University of Singapore (NUS) and the Naval Postgraduate School (NPS) in analyzing and testing a 3 to 5 μm thermal imager and exploring the use of narrow band filters to enhance detection, recognition and discrimination of targets of interests. This project was in its first year when this study was completed.

B. SCOPE OF STUDY

Test techniques were first developed to characterize both an existing thermal imager (TI), the Cincinnati Electronics IRRIS-256LN, and a newly purchased TI, the Merlin InSb Laboratory Camera. This characterization also served as an acceptance test for the new TI. The performance characterization was based on common performance parameters such as signal transfer function (SiTF), noise equivalent temperature difference (NETD), contrast transfer function (CTF), modulation transfer function (MTF) and minimum resolvable temperature difference (MRTD). Next, a survey was made to select suitable narrow band filters for research on target discrimination improvement. For the purpose of this research, the filters were chosen to capture the unique signature of a fast moving air target. These filters were subsequently purchased and installed in the Merlin camera for further experimentation. Using the previously developed test techniques for performance characterization, system performance with these installed filters was compared with operation in the original 3 to 5 μm band. Finally, some images of a propane flame acquired using these narrow band filters were analyzed. The image acquisition and analysis were carried out using commercial image acquisition software, IRvista 2.51. Specifically, the potential of using narrow band filters for discrimination of targets was discussed extensively.

C. PREVIOUS WORK DONE

Performance parameter measurement techniques for TI have been generally established over the last few decades. These techniques are well recorded and explained in textbooks such as those published by Holst [2]. Of all performance indicators, the MRTD measurement is seen in this field as the principal performance parameter of a TI system. However, this measurement is subjective and non-repeatable. Significant effort has also gone into prediction of the MRTD frequency response from various subsystem transfer functions and other related parameters. An example is the development of Visibility Model II [3].

This model was developed for second generation TI and it included sampling and aliasing issues without assumptions about the observer. Edwards [4] also developed an objective measurement of MRTD, and Pieper [5] found general agreement between the predictive VISMOT II model with objective MRTD measurement. However, these objective MRTD measurements were found to be generally higher than the subjective MRTD, suggesting that the human eye-brain process is relatively more efficient in identifying signals in a noisy environment.

In the military, IR sensors are widely employed in imaging systems, missile seekers and tracking systems. The key to these applications is the ability to detect, recognize and discriminate targets of interest. On the other hand, those who perform research on IR countermeasures have the objective to deny these possibilities. Common countermeasures include the use of flares and chaff. These measures generally operate by having thermal signatures greater than the targets and hence, attempt to seduce the thermal sensors to track on them. This can be countered with the use of polarized spectral imaging or multi-spectral band sensors. Tung [6] demonstrated that images recorded in the laboratory with horizontal and vertical polarization depict a contrast enhancement differing with varied aspect of the target. In multi-spectral band sensing, polarization filtering has the potential to identify specific target signatures from other thermal sources by correlating images obtained in various bands. It can also be used to enhance image quality by fusing selected important features of various images from various spectral ranges. Multi-spectral sensors have been widely used in space and geological exploration. These sensors usually use a wide range of spectrum, spanning from the visible range to the far infrared region. The main advantage of these systems is that they can provide details in different spectral bands, and information can be derived separately or jointly through data fusion. This is possible due to the fact that different objects radiate differently in different spectral bands. Similarly, information from different narrow spectral bands can be collected and fused or correlated to identify unique signature of targets. Northrop Grumman Electronic Systems [7] has developed a multi-spectral seeker for boost phase intercept for incoming missiles. It uses four narrow spectral bands for

correlation and hence, to discriminate intended targets. Other applications of multi-spectral sensors include infrared temperature measurements of industrial materials. Specific band-pass filters are used to eliminate interfering radiation from surroundings while capturing the desired spectral radiance from the object of interest. An example is the infrared measurement of base metal temperature in gas tungsten arc welding published by Farson and Richardson [8]. Experimental results showed that radiations from both the arc and hot tungsten electrode were important sources of IR emission from the base metal. Attenuation of the interfering radiation was carried out using a bandpass optical filter.

II. FUNDAMENTALS

This chapter serves to present the basic theories of infrared technology necessary for this thesis to be understood.

A. ELECTROMAGNETIC SPECTRUM

The infrared frequency wave band lies between the visible and the microwave frequencies within the electromagnetic spectrum (Figure 2.1). Infrared systems operate in a narrow region approximately from 0.7 μm to 15 μm . [9]. This region is further subdivided into the near infrared (NIR), short-wave (SWIR), mid-wave (MWIR) and long-wave infrared (LWIR). The NIR is characterized by wavelengths from 0.7 μm to 1.1 μm and SWIR has wavelength from 1.1 μm to 2.5 μm . The radiance in these two regions where image intensifiers operate includes mostly reflected solar radiation. Here the reflected ambient light from objects is detected by photo-emissive process with amplification of the emitted free electron flux. The MWIR is characterized by wavelength from 2.5 μm to 6.0 μm and LWIR from 6.0 μm to 15 μm . These two longer wave regions are where thermal imagers detect the thermal emission from observed objects. Detection is typically by absorption of the energy, producing charge carriers internally across in the band gap of semiconductors. These wave bands are also termed the “Thermal Imaging” range, where Forward Looking Infrared (FLIR) and other infrared tracking systems work. However, due to atmospheric attenuation and the detection sensitivity of most thermal detectors, the useful thermal imaging sub-bands for MWIR and LWIR are typically 3 μm to 5 μm and 8 μm to 12 μm respectively.

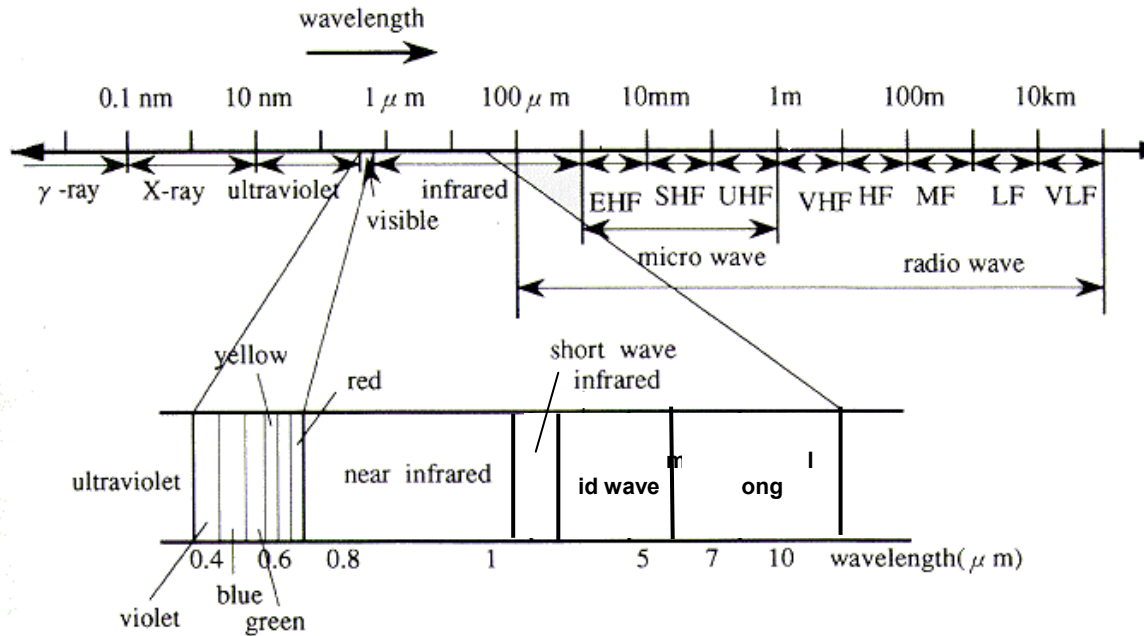


Figure 2.1. Electromagnetic Spectrum.
(After [10])

There are some common definitions or terms used to describe the main laws of infrared radiation.

- Emissivity (ϵ) is defined as the ratio of the radiant exitance or radiance of a given body to that of a black body.
- Blackbody is an object which absorbs all thermal radiation that impinges upon it at any wavelength. A black body, by definition, has an emissivity equal to unity ($\epsilon = 1$).
- Gray body is an object whose emissivity is high and fairly constant with wavelength.
- Radiant energy is the total energy radiated or absorbed.
- Radiant flux or radiant power is the total energy per unit time (t) radiated or absorbed.
- Radiant exitance or emittance is the radiant flux density leaving the target surface per unit area (A).

- Radiant incidence or Irradiance is the radiant flux density incident on target surface per unit area.
- Radiant intensity is defined as radiant power exiting a point source along a given direction within a unit solid angle (Ω).
- Radiance in a given direction is the radiant power per unit area per unit solid angle leaving or incident on an area projected perpendicular to the direction of energy flow.

Table 2.1 summarizes these commonly used infrared quantities and their units.

Quantity	Definition	Units	Symbol
Radiant energy	Total radiated energy	Joules	Q
Radiant power	$\partial Q / \partial t$	Watts	P
Radiant exitance	$\partial P / \partial A$	Watt/m ²	M
Radiant incidence	$\partial P / \partial A$	Watt/m ²	E
Radiant intensity	$\partial P / \partial \Omega$	Watt/sr	I
Radiance	$\partial^2 P / \partial A \partial \Omega$	Watt/m ² sr	L

Table 2.1. Definition of Radiometric Quantities. (After Lloyd, 1996).

B. LAWS OF THERMAL RADIATION

1. Planck's Blackbody Radiation Law

The spectral radiant exitance of an ideal black body source whose absolute temperature is T and wavelength of radiation is λ (in meters), can be described by Planck's blackbody radiation law [9]:

$$M_b(\lambda, T) = \frac{c_1}{\lambda^5} \left(\frac{1}{e^{(c_2/\lambda T)} - 1} \right) \quad (2.1)$$

where the first radiant constant $c_1 = 3.7418 \times 10^8 \text{ watt-}\mu\text{m}^4/\text{m}^2$ and the second radiation constant is $c_2 = 14388 \mu\text{m-K}$. Figure 2.2 shows Planck's law graphically.

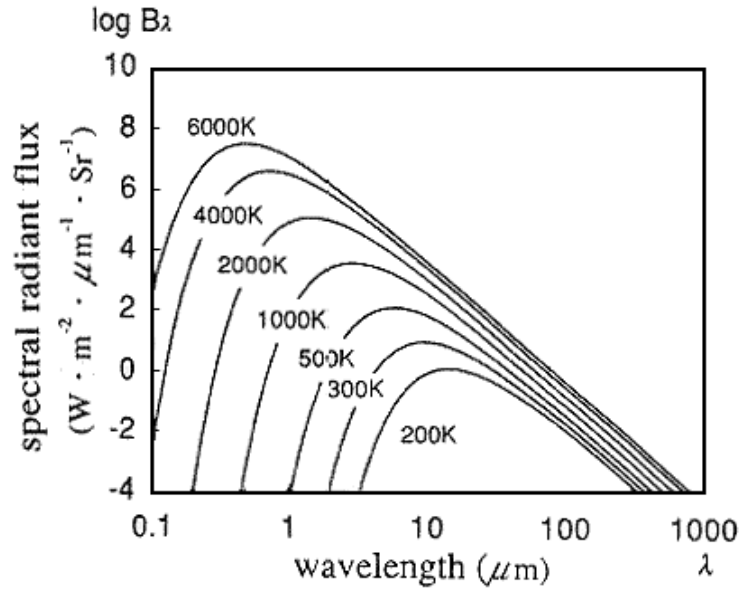


Figure 2.2 Planck's law plotted graphically.
(From [11])

2. Wien's Displacement Law

By differentiating Planck's formula with respect to the wavelength (λ), and solving for the maximum, Wien's law gives the wavelength where the peak radiation occurs at a given temperature. Wien's Law is stated as:

$$\lambda_{\max} = \frac{2898}{T} \quad (2.2)$$

where λ_{\max} is the wavelength where the peak of radiation occurs in μm .

3. Stefan-Boltzmann Law

Total radiation emittance of a blackbody can be obtained by integrating Planck's Law over the entire spectrum. The result is known as the Stefan-Boltzmann Law and is formulated as follow:

$$W_b = \sigma T^4 \quad (2.3)$$

where W_b = Total radiant emittance of a black body
 σ = Stefan-Boltzmann constant (5.67×10^{-8} Watt/m² K⁴)
 T = Absolute temperature (K)

For use with a non-blackbody source, Eq. (2.3) is given as the form:

$$W_b = \varepsilon \sigma T^4 \quad (2.4)$$

where ε is the effective emissivity of the non-blackbody source.

C. TARGET TO BACKGROUND CONTRAST

Lloyd [12] stated that scene radiation along a line of sight (LOS) from the source to the imager system arises from four mechanisms. They are self emission, transmission of emission from objects behind the scene, reflection of remote emissions from objects in front of the source, and the scattering and/or diffraction of all of these from outside the LOS into the LOS by the intervening atmosphere.

The radiant characterization of a source relative to its background is called the source signature. Signature is composed of five elements: the differences in intensity between source and background with insignificant spectral differences (contrast), differences in intensity with wavelength (color), differences in polarization, differences in the spatial correlation length and the intensity relative to surrounding scene sources (conspicuity), and the time variations (motion and intensity modulation). The two source signatures that are of particular interest in this study are contrast and conspicuity. Specifically, this contrast is the difference between the irradiance received from the target and the irradiance received from its surrounding objects or background. In general, contrast relative to background can be defined [9] as:

$$C_o = \frac{I_{target} - I_{background}}{I_{background}} \quad (2.5)$$

where:

I_{target} = irradiance from target

$I_{background}$ = irradiance from background

Alternatively,

$$C_o = \frac{I_{target} - I_{background}}{I_{target} + I_{background}} \quad (2.6)$$

It is sometimes useful to quantify imagers when being compared in terms of contrast improvement. This can be achieved by comparing absolute contrast which is defined as:

$$\Delta I = I_{target} - I_{background} \quad (2.7)$$

Hence, the improvement factor between images 1 and 2 is given by:

$$F = \frac{\Delta I_1}{\Delta I_2} \quad (2.8)$$

D. SENSITIVITY AND RESOLUTION LIMITS

Most imaging quality discussions involve either spatial resolution or sensitivity. Resolution implies something about the smallest details that can be perceived in an image [9]. It provides an estimate for a target range which is given by:

$$Range = R = \frac{target\ size}{resolution} \quad (2.9)$$

However, resolution does not include the effects of system noise.

Sensitivity, on the other hand, deals with the smallest signal that can be detected. It is usually taken as the signal that produces unity signal-to-noise (SNR) ratio at the signal output. Sensitivity is dependant upon the light-gathering properties of the optical system, the responsivity of the detector, and the noise of the system. It is independent of the resolution. Sensitivity provides another estimate for SNR [9].

$$SNR = \frac{(\tau_{atm-ave})^R \Delta I}{system\ noise} \quad (2.10)$$

where:

ΔI = intensity difference between target and background

$\tau_{\text{atm-ave}}$ = average atmospheric attenuation coefficient

R = range

For infrared imaging systems, the target-background intensity difference is specified by a differential temperature (ΔT). The system noise is taken to be the noise equivalent temperature difference (NETD). This approximation is valid only for those targets whose angular subtense is large compared to the system's resolution at the calculated range.

Overall system response depends on both sensitivity and resolution. As shown in Figure 2.3, the minimum resolvable temperature (MRT) difference is bounded by sensitivity and resolution considerations. Figure 2.4 shows a comparison of two different systems. In the figure, system A has better sensitivity as it has lower MRT at low spatial frequencies. In other words, it can detect targets at a lower temperature difference. On the other hand, system B has better resolution as it can resolve larger spatial frequencies (smaller details) as compared to system A. They have similar performance at the mid spatial frequencies. This example illustrates that neither sensitivity nor resolution alone, or other single parameter, can be used to compare systems. It depends largely on their applications.

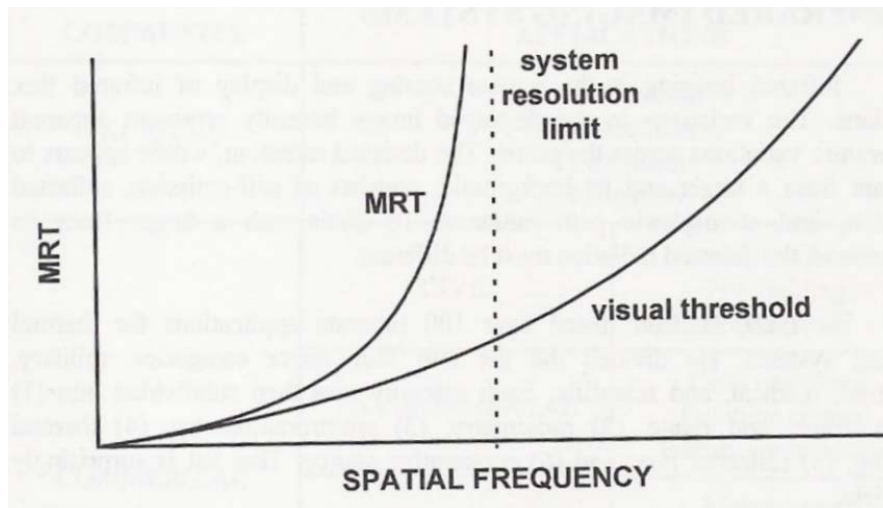


Figure 2.3 MRT is bounded by the system's resolution and by visual sensitivity limit. (From [9]).

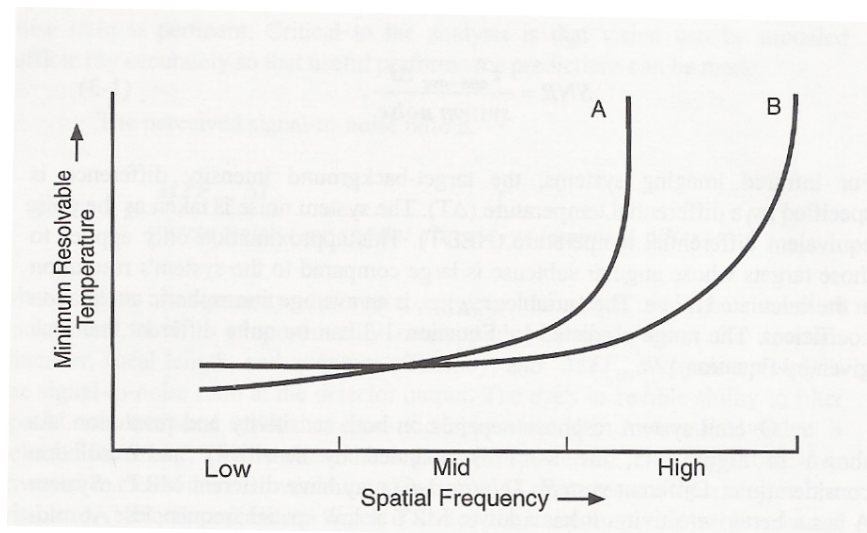


Figure 2.4 Two systems with different MRTs. (From [9]).

THIS PAGE INTENTIONALLY LEFT BLANK

III. PERFORMANCE PARAMETERS OF INFRARED IMAGING SYSTEMS

There is no single parameter that can adequately be used to compare the performance of infrared imaging systems [2]. This chapter attempts to present the common characterization of these systems. This includes measuring the signal transfer function, noise equivalent temperature difference, contrast transfer function and minimum resolvable temperature difference. The Modulation transfer function can be calculated from CTF.

In this characterization, all measurements can be considered as output/input transformations. The output is typically a voltage change on the analog video or the change in monitor luminance. The input may be temperature difference, target angular subtense or target spatial frequency.

A. SIGNAL TRANSFER FUNCTION (SITF) AND NOISE EQUIVALENT TEMPERATURE DIFFERENCE (NETD)

SiTF is the slope of the linear portion of the response function of a system. The responsivity function is defined as the output to input transformation in which the target size is fixed and the target intensity is varied. It is typically S-shaped. (Figure 3.1). For many systems, the electronics have a limited dynamic range compared to the detector and the output is centered about some average value. The dynamic range is defined as the range of input signal that gives a linearly related output signal. Saturation in the positive and negative directions about this average value is typically limited electronically by the dynamic range of an amplifier or analog-to-digital (A/D) converter.

Noise is defined in the broadest sense as any unwanted signal components that arise from a variety of sources. The rms noise voltage can be referred to the input that produces an SNR of unity. NEDT is a measure only of system sensitivity. It is an excellent tool for production testing to verify performance but it is a poor system-to-system performance parameter. The system noise signal can be measured as the output signal when no useful input

signal is applied. Once SiTF is obtained from the responsivity function, the NETD can be calculated as follows

$$NETD = \frac{\Delta V_n}{SiTF} \quad (3.1)$$

where

$$SiTF = \frac{\Delta V}{\Delta T} = \text{slope of responsivity function}$$

ΔV_n = output root mean square (rms) noise voltage

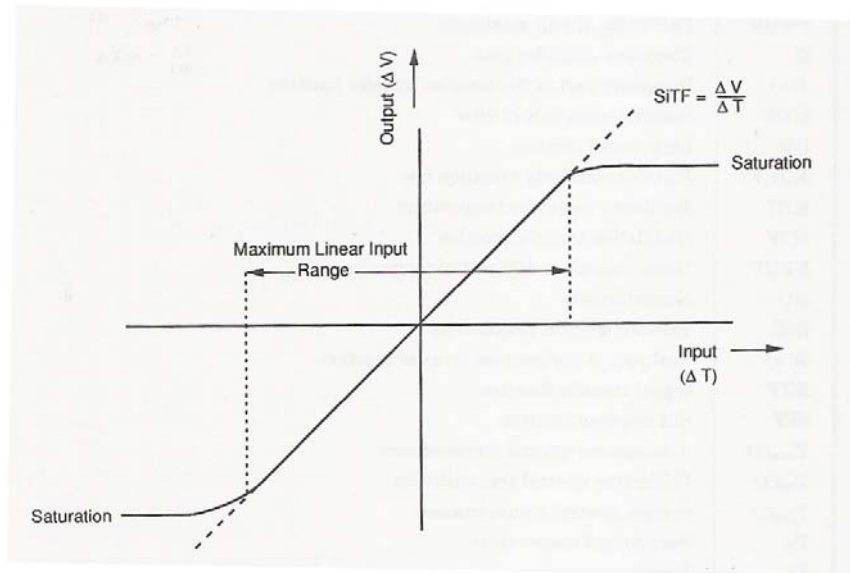


Figure 3.1 Typical responsivity function illustrating the SiTF.
(From [2])

B. CONTRAST TRANSFER FUNCTION (CTF) AND MODULATION TRANSFER FUNCTION (MTF)

The MTF is a fundamental parameter used for system design, analysis and specifications. Methods to measure MTF depend on both optical and electronic signal considerations. MTF is the system's response to spatial sinusoidal signals. MTF is a measure of how faithfully the system reproduces the scene. As the MTF decreases, scene details associated with those specific spatial frequencies are reproduced with lower contrast. The limit, where MTF approaches zero, is the system cutoff. The system can detect signals whose spatial frequencies are above cutoff but cannot faithfully reproduce them. From a design point of view, the MTF should be as "high" as possible over spatial frequencies of interest.

MTF can be obtained by measuring the response to sinusoidal targets. Alternatively, this can be done by measuring square bar targets to obtain the CTF and mathematically converting to the sinusoidal response (MTF) using a series approximation. Modulation is defined as:

$$Modulation = \frac{B_{\max} - B_{\min}}{B_{\max} + B_{\min}} \quad (3.2)$$

where B_{\max} and B_{\min} are the maximum and minimum intensity levels defined in Figure 3.2. MTF is given by:

$$MTF = \frac{image\ Modulation}{object\ Modulation} \quad (3.3)$$

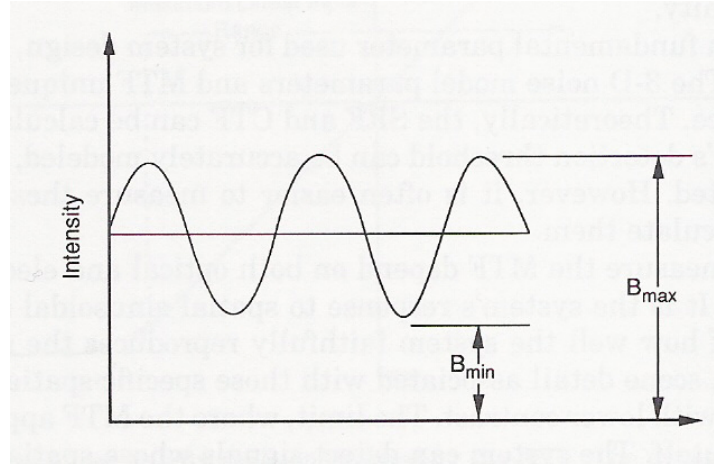


Figure 3.2 Definition of modulation (From [2])

Figure 3.3 shows a plot of MTF as a function of spatial frequency. Usually MTF is calculated from CTF due to the ease of having bar targets as input signal. A square wave can be expressed mathematically as a series of sinusoids. The amplitude of the square wave at frequency f_x is an infinite sum of sinusoidal amplitudes. Conversely, the sine wave amplitude at frequency f_x can be expressed as an infinite sum of square-wave amplitudes. Therefore, MTF at a particular frequency f_x can be calculated using the following series approximation.

$$MTF(f_x) = \frac{\pi}{4} \left| CTF(f_x) + \frac{CTF(3f_x)}{3} - \frac{CTF(5f_x)}{5} + \frac{CTF(7f_x)}{7} - \frac{CTF(9f_x)}{9} + \dots \right| \quad (3.4)$$

Figure 3.4 shows the relationship between MTF and CTF graphically. Note that the 'zero' spatial frequency value can be determined by measuring the response to a step input, such as a large target.

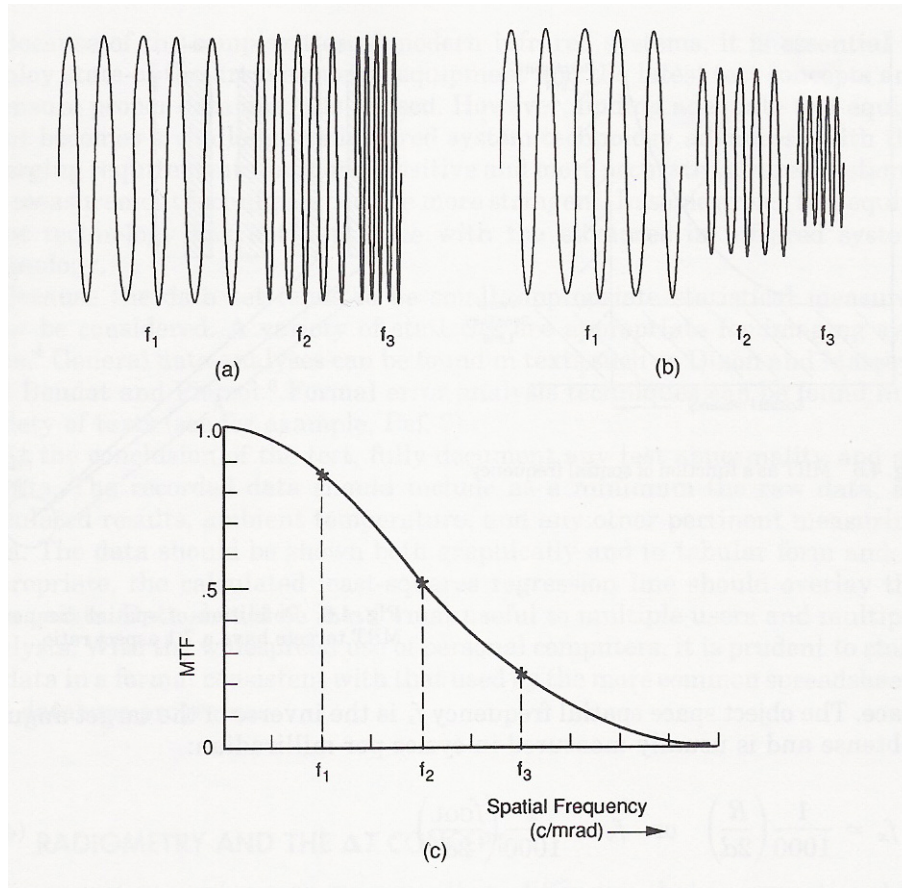


Figure 3.3 Definition of modulation transfer for three spatial frequencies: (a) input (object) modulation, (b) output (image) modulation, and (c) the MTF. (From [2])

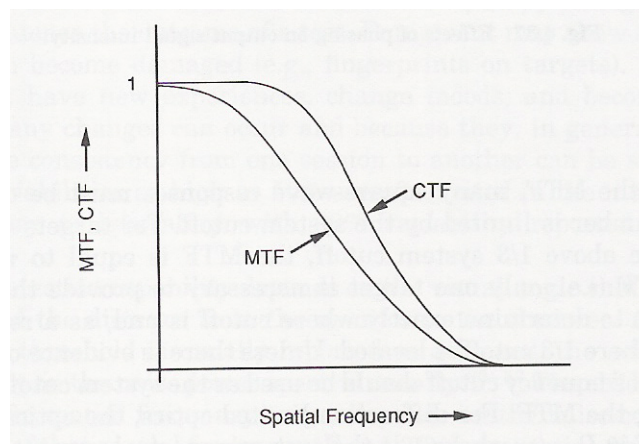


Figure 3.4 Relationships between CTF and MTF. (From [2]).

C. MINIMUM RESOLVABLE TEMPERATURE (MRT) DIFFERENCE

MRT is widely used and accepted as the most important laboratory measure of the performance of an imager. It combines visual sensitivity and resolution of a system in one single test (Figure 3.5). Visual sensitivity is the measure of the lowest SNR that is acceptable to the eye. The resolution limit is related to the smallest detail that can be discriminated. However, MRT measurement is subjective in nature. It depends on the observer's ability to resolve a four-bar pattern embedded in noise, and this largely depends on the decisions made by observer. The MRT measurement inevitably varies with training, motivation and visual capacity of the observer.

Although MRT is generally subjective when determined experimentally, Shumaker, Wood and Thacker [13] proposed a mathematical representation as follows:

$$MRT(v) = \frac{2 SNRT NET \rho_x^{1/2}}{MTF(v)} \left[\frac{v^2 \Delta x \Delta y}{L} \right]^{1/2} [t_e F_r N_{os} N_{ss}]^{-1/2} \quad (3.5)$$

where

SNRT	the perceived signal-noise-ratio threshold
v	the spatial frequency characterizing the MRT target
MTF	the system modulation transfer function
L	the length-to-width ratio of a bar in the bar chart
t_e	the eye integration time
F_r	the system frame rate in Hz
N_{os}	the overscan ratio
N_{ss}	the serial scan ratio
NET	the system noise equivalent temperature in K
ρ_x	the noise filter factor
Δx	the in-scan detector subtense in mrad
Δy	the cross-scan detector subtense in mrad

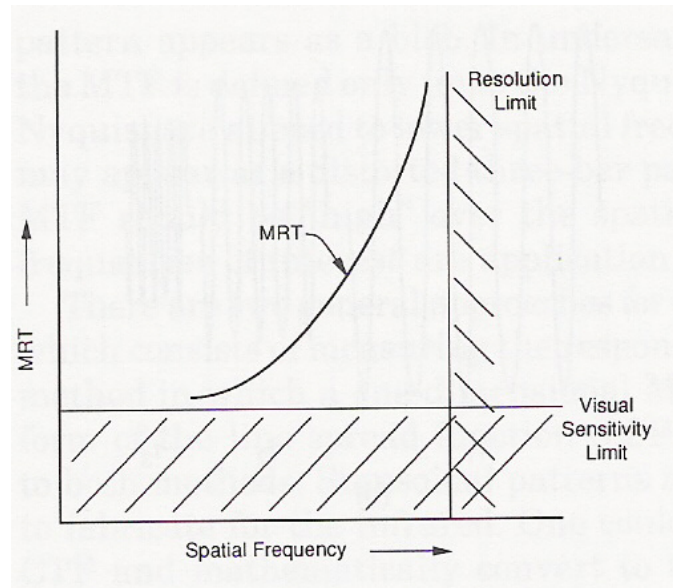


Figure 3.5 MRT as a function of spatial frequency.
(From [2])

Note that object space spatial frequency is commonly used to characterize the MTF, CTF and MRT. It is the inverse of the four-bar target angular subtense and is usually measured in cycles per milliradian as shown. (Figure 3.6).

$$f_x = \frac{1}{1000} \left(\frac{R}{2d} \right) \quad (3.4)$$

where

$2d$ = spatial extent of one cycle (one bar and one space)

R = distance from the entrance aperture of imager to the target.

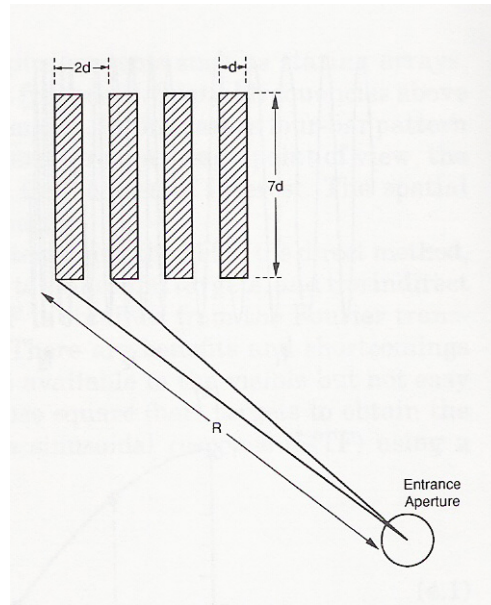


Figure 3.6 Definition of spatial frequency. The MRT 4-bar target is a square pattern. Each bar has a 7:1 aspect ratio. (From [2]).

IV. CHARACTERIZATION OF THERMAL IMAGERS

In this chapter, test procedures for characterizing the performance parameters of a thermal imager are developed and evaluated. Both the existing Cincinnati Electronics IRRIS-256LN and the newly purchased Merlin InSb Laboratory Camera were tested and compared using these performance indicators. These comparisons also served as an acceptance test for the Merlin camera for its subsequent use in research on narrow band images.

A. SYSTEM SPECIFICATIONS

1. Cincinnati Electronics IRRIS-256LN

The existing Cincinnati Electronics IRRIS-256LN is a generation III cooled mid wave ($3 - 5 \mu\text{m}$) thermal imager (Figure 4.1). It uses a hybrid focal plane array (FPA) with 256×256 Indium Antimonide (InSb) detectors. This system is cooled to 77K using liquid nitrogen. The InSb detector has a relatively high quantum efficiency of 80% and is relatively sensitive, with a nominal sensitivity of 0.025K [6].



Figure 4.1 The Cincinnati Electronics IRRIS-256LN.

2. Merlin InSb Laboratory Camera

The newly purchased Merlin InSb Laboratory Camera (Figure 4.2) is a liquid nitrogen cooled mid-wave infrared camera that is based on an ISC9705 based FPA [14]. Its array consists of 320 x 256 InSb detectors. It has a standard 3 – 5 μm bandpass although it also supports bandpass from 1.5 to 5.0 μm . The laboratory imager also allows changing of Dewar windows and cold filters within the dewar. The imager allows a maximum of four filters to be installed at any one time. The filter wheel configuration facilitates switching of filters without the need to access the interior and this avoids contamination to the Dewar. In terms of sensitivity, it has a specification for NEDT to be typically less than 0.018K. Other technical details can be found in Appendix A.

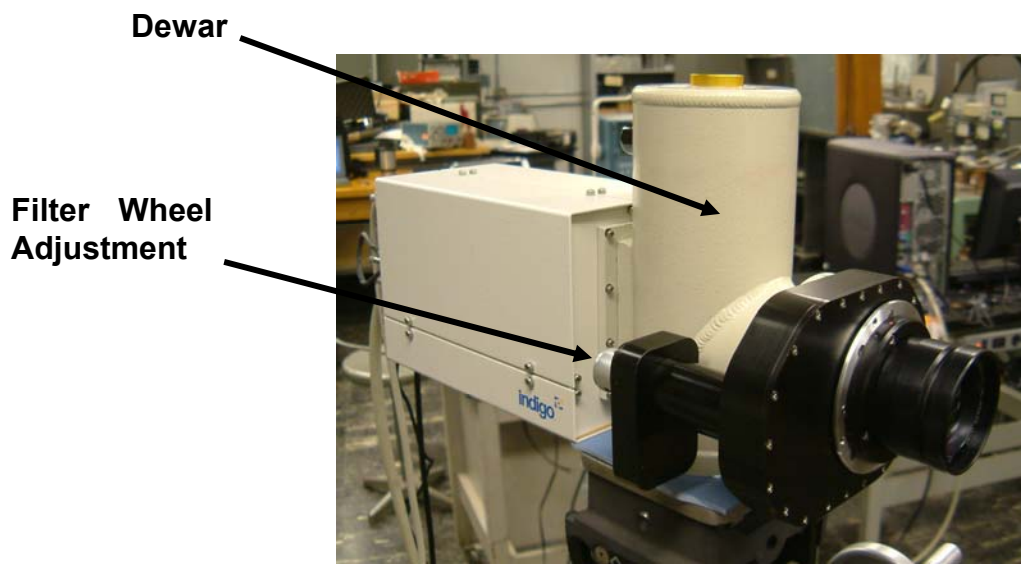


Figure 4.2 The Merlin InSb Laboratory Camera.

B. LABORATORY SET UP AND EXPERIMENTAL PROCEDURES

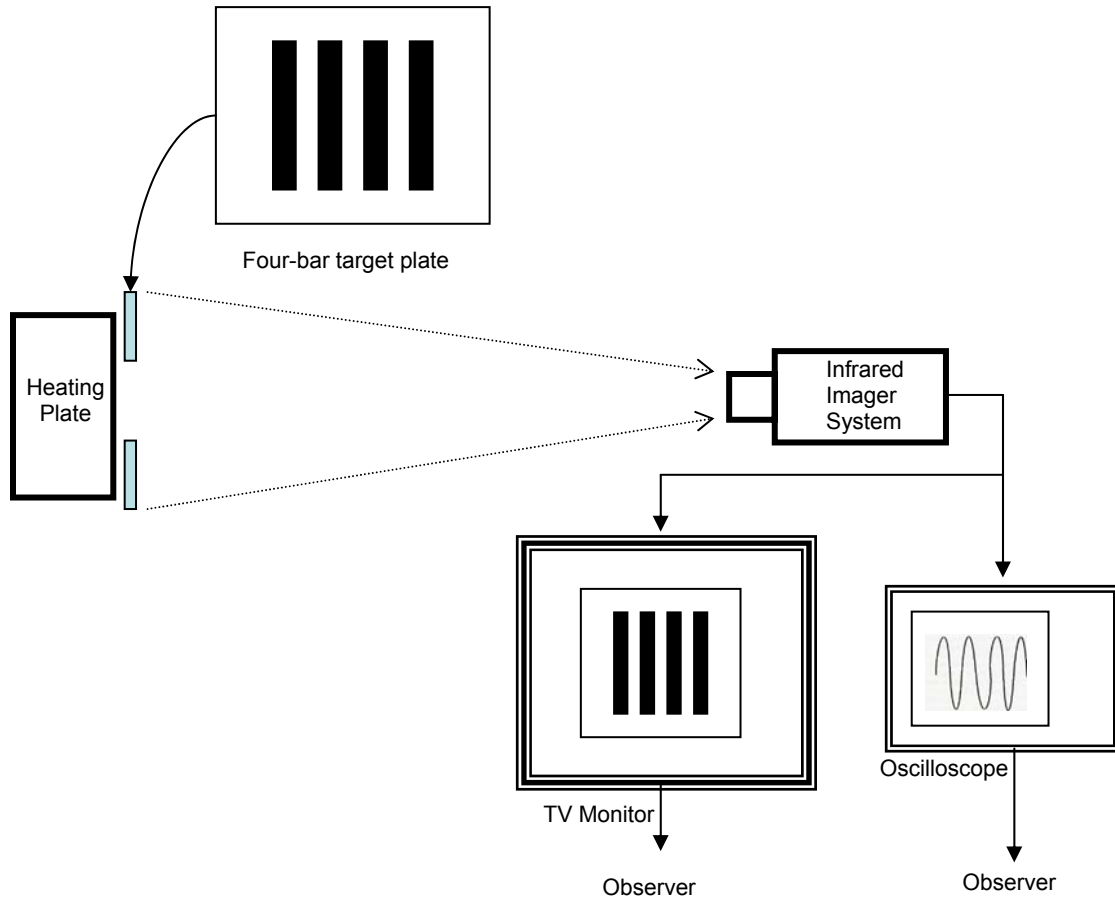


Figure 4.3. Equipment setup schematic.

Most of the experimental procedures for these characterizations were closely referenced from Holst [2]. Modifications to the test procedures were made to suit existing laboratory equipment and settings.

The general experimental setup for all the experiments is shown schematically in Figure 4.3. The four bar target consists of a heating plate and a target plate. The target plate comes with different sizes of standard four slot MRTD patterns. Each bar has an aspect ratio of 7 to 1. With 4 bars and 3 spaces, each 4-bar pattern is essentially a square. The various bar sizes allow measurement with different spatial frequencies. Both the heating plate and target plate are each fitted with a thermocouple for their respective temperature

measurement. Heating elements can be attached to either plate to increase its temperature. Figure 4.4 shows the actual experimental setup.

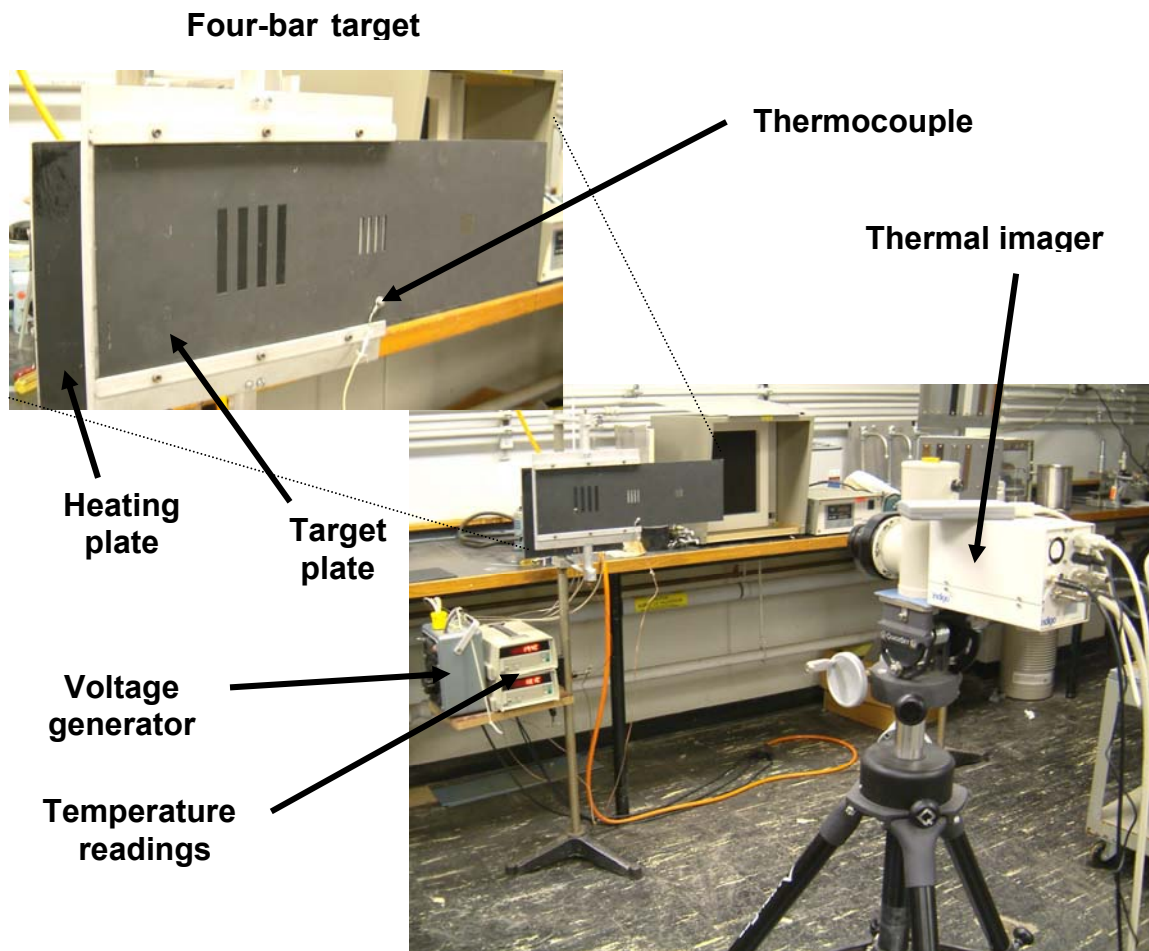


Figure 4.4 Actual experimental setup.

1. Signal Transfer Function and Noise Equivalent Temperature

In this experiment, a fixed 4-bar target plate of square width 70 mm was used. The imager was placed close enough such that the target plate covered more than 80% of the field of view (FOV) of the imager.

The temperature of the heating plate (T_b) was first raised while the temperature of the target plate (T_a) remained at room temperature (18.2 °C). Temperature difference (ΔT) between the two plates was given by the following equation:

$$\Delta T = T_b - T_a \quad (4.1)$$

By definition of equation (4.1), this gave a positive ΔT value. Once ΔT was stabilized, the corresponding difference in output voltages (ΔV) was obtained from the oscilloscope connected to the camera. The experiment was repeated for different ΔT until the ΔV values were observed to be stabilized about a fixed value. This gave the average value when the system saturated in the positive direction. The heating plate was subsequently allowed to return to room temperature. Thereafter, the target plate was heated to give a negative ΔT value. The target plate was heated with two electrical heating elements attached to the front plate. The temperature sensor was attached directly to one of the gaps of the 4-bars to obtain the temperature of the bar pattern. The experiment was repeated for different ΔT until the ΔV values were observed to be stabilized. This gave the average value when the system saturated in the negative direction.

The experimental results were then plotted with ΔV against ΔT to obtain the responsivity curve of the system. Subsequently, SiTF and NETD were obtained using equation (3.1).

2. Contrast Transfer Function and Modulation Transfer Function

In this experiment, 4-bar targets of various dimensions were used to give a variation in spatial frequencies while keeping the temperature constant. The temperature of the heating plate was first raised and maintained at 1 °C throughout the experiment. For each spatial frequency, the corresponding peak output voltage, B_{max} , and output voltage, B_{min} , due to background or in this case, target plate, were recorded. This procedure was repeated for a variety of spatial frequencies (Figure 3.2).

CTF and MTF were then calculated for each spatial frequency according to equation (3.2) and (3.4) respectively. Normalized CTF and MTF values were used to plot against spatial frequencies for ease of comparison and use. Curves were then generated to fit these experimental points. The intersection between the curve and the x-axis gave the system cut-off spatial frequency.

Guimaraes [20] recommended the use of sinc function of the following form for CTF curve fitting.

$$y = \sin c \left(\frac{f_x}{f_c} \right)^x, \quad (4.1)$$

where

f_c is the cut off frequency

f_x is the spatial frequency

x is a curve fitting parameter to be determined

3. Minimum Resolvable Temperature Difference

The observer's ability to resolve various spatial frequencies was evaluated in this setup. The observer viewed the image as presented on the TV monitor screen and was allowed to adjust the settings of the monitor and thermal imager to best acquire the target. This included the focusing, contrast and brightness settings of the monitor and imager. There was also no restriction on the dwell time. As a guide, the observer must be able to count the number of vertical bars and the bars must appear as having the same width.

Beginning with the largest target, which had the smallest spatial frequency, the temperature of the blackbody was slowly increased. Temperature was allowed to stabilize at every 0.1 °F interval before increasing it again. The temperature at which the observer was able to resolve the 4 bars was then recorded. The difference in temperatures between the blackbody and plate gave the MRT value for each particular spatial frequency. This procedure was repeated for different target sizes or different spatial frequencies. The distance between the imager and the target was also recorded for the calculation of angular spatial frequencies. Spatial frequency for each target was calculated using equation (3.4). Finally, these temperature differences were plotted against spatial frequency (f_s). The asymptote of this curve gives the system cut-off frequency.

MRT can be determined from a complete set of engineering parameters of the system, but is more often deduced from measurements. The Hepfer fitting function [15] preserves the shape of the MRT curve, matched to data for a specific camera by optimization of the empirical constants. The Hepfer form is given as follows:

$$MRT = SL + ((SL \times 2 \times f_s) / 2.646) \exp(1.571 \times ER^2 \times f_s^2) \quad (4.3)$$

For ease of curve fitting, this parametric equation can be reduced to

$$MRT = A + B \times f_s \times \exp(C \times f_s^2) \quad (4.4)$$

where $A = SL$ (can be determined by observation when f_s tends to zero)
 $B = (SC \times 2 \times f_s) / 2.646$
 $C = \exp(1.571 \times ER^2)$

C. EXPERIMENTAL RESULTS AND ANALYSIS

The experimental results are presented and analyzed in this section. A comparison of the imagers is also given.

1. Signal Transfer Function and Noise Equivalent Temperature

Table 4.1 shows the experimental Signal transfer results for the Cincinnati thermal imager. These results are plotted and shown in Figure 4.5. The dynamic range (linear portion) for the Cincinnati was found to be from 1.6 °C to -1.6 °C. The rms noise voltage for the system was found to be 16.0 mV. This noise value was obtained from the oscilloscope output when the input signal was zero. SiTF and NETD were then calculated to be 70.6 mV/°C and 0.23 °C respectively using equation (3.1). Note that these values correspond to the overall SiTF and NETD of the system. This system includes all electronics from the imager to the output of the oscilloscope.

Table 4.2 and Figure 4.6 show the corresponding experimental results for the Merlin thermal imager. The dynamic range for Merlin was evaluated to be approximately 3.0 °C to -3.0 °C. The SiTF and NETD are 56.7 mV/°C and 0.28 °C respectively. Note that the NETD of the Merlin imager is quoted as less than 0.025 K by the manufacturer. (Appendix A). The measured NETD is greater by more than a factor of ten than the manufacturer's specification number. The

measured value is an analog value representative of the observed signal from the oscilloscope screen. This value should be read as characterizing the display and measurement system rather than the camera. This system in its present form is unsuitable for measuring NETD for this imager.

The SiTF measurement is carried out so that the subsequent measurements of CTF are made within the dynamic range of the TI measurement system. From the experiments, the Merlin TI is found to have greater dynamic range. In other words, it gives a better linearity in measuring temperature variation over a wider range. However, the SiTF for the Cincinnati imager seems to be greater than that of the Merlin camera. This means that the Cincinnati TI is more sensitive or responsive within its narrow dynamic range. And with greater sensitivity, the NETD of the Cincinnati is found to be lower than that of the Merlin. NETD is 0.23°C for the former compared to 0.28°C of the latter. Nevertheless, it should be noted that this is the system's overall noise equivalent measurement and is not that of the respective thermal imager alone. The variations found between the two imagers are considered inconsequential because Generation III imagers have typical NETD values in the range of one hundredth of a degree C. The main bulk of noise is probably due to the other electronic systems such as the television monitor and oscilloscope. Finally, the experimental temperature measurement is constrained by the precision of the thermocouples to 0.1°F resolution. This is inadequate to measure the typical NETD of a generation III thermal imager which is in the order of mK. A higher resolution temperature measurement system has to be used to improve this experimental evaluation.

ΔT (°C)	ΔV (mV)
-3.0	-104.0
-2.5	-106.0
-2.0	-106.0
-1.5	-102.0
-1.0	-72.0
-0.5	-34.0
0.5	38.0
1.0	76.0
1.5	106.0
2.0	110.0
2.5	104.0
3.0	104.0

Table 4.1 SiTF experimental results for Cincinnati thermal imager.

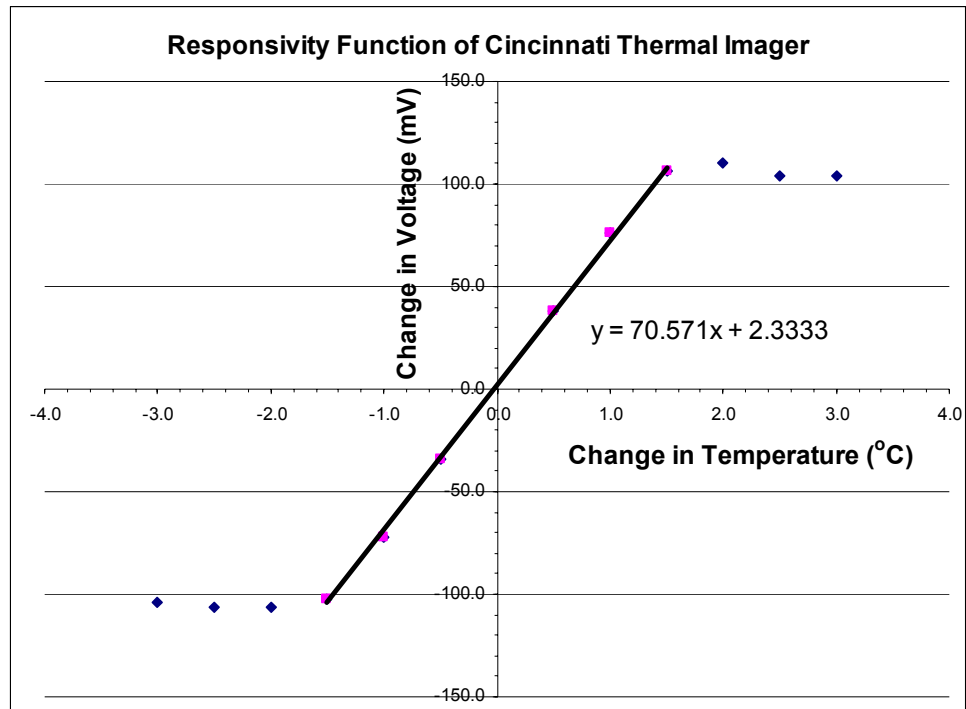


Figure 4.5 Measured Responsivity curve for Cincinnati thermal imager.

ΔT (°C)	ΔV (mV)
-4.0	-162.0
-3.5	-162.0
-3.0	-156.0
-2.5	-146.0
-2.0	-130.0
-1.5	-110.0
-1.0	-74.0
-0.5	-32.0
0.5	30.0
1.0	56.0
1.5	80.0
2.0	106.0
2.5	132.0
3.0	166.0
3.5	170.0
4.0	168.0

Table 4.2 SiTF experimental results for Merlin thermal imager.

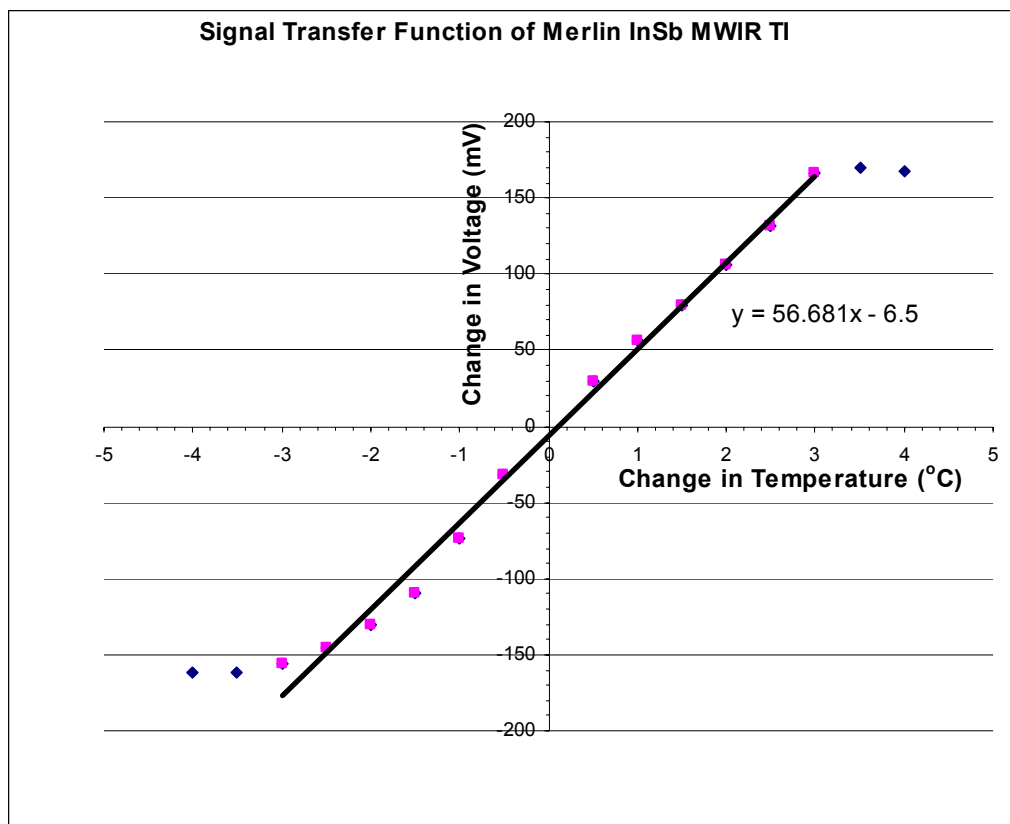


Figure 4.6 Measured Responsivity curve for Merlin thermal imager.

2. Contrast Transfer Function and Modulation Transfer Function

The experimental CTF results for the Cincinnati thermal imager are shown in Table 4.3 and plotted in Figure 4.7.

F_s (cycle/mrad)	B_{max} (mV)	B_{min} (mV)	B_{max} - B_{min} (mV)	B_{max} + B_{min} (mV)	CTF	Normalized CTF
0.000	472	390	82	862	0.09513	1.0000
0.092	464	386	78	850	0.09176	0.9646
0.183	462	386	76	848	0.08962	0.9421
0.305	448	386	62	834	0.07434	0.7815
0.377	408	380	28	788	0.03553	0.3735
0.458	402	380	22	782	0.02813	0.2957
0.582	402	380	22	782	0.02813	0.2957

Table 4.3 CTF for Cincinnati thermal imager.

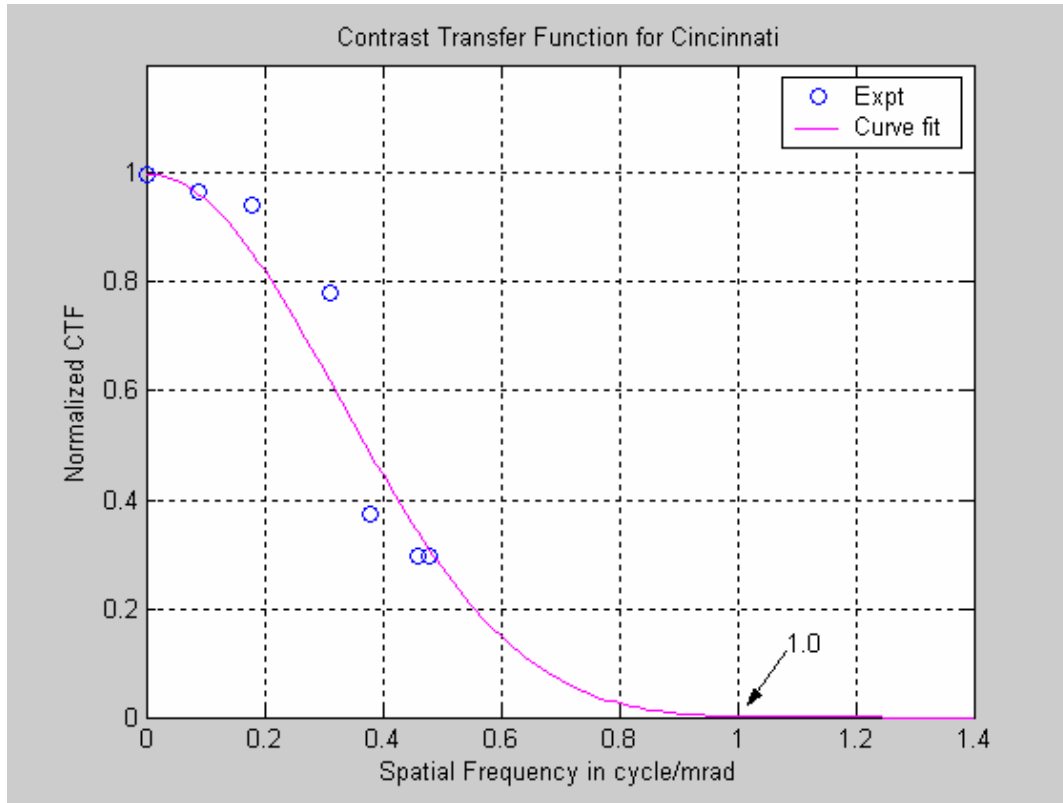


Figure 4.7 Plot of CTF result for Cincinnati thermal imager.

Equation (4.1) was used to curve fit the experimental results. A value of 1.05 cycle/mrad was first used as cut-off frequency. This was referenced from a previous study of the MRT value of the same system [6]. However, through an iterative process, by comparing the mean square values, a cut off frequency of 1.25 cycle/mrad was found to best fit the curve. The corresponding x value was found to be 4.612. From the plot, based on intersection of the curve with the x -axis, a more accurate estimate for the cut-off frequency was found to be approximately 1.0 cycle/mrad. This should not be confused with the initial estimate of 1.25 cycle/mrad which was used for curve fitting.

MTF was then calculated using equation (3.4). Both CTF and MTF are plotted in Figure 4.8.

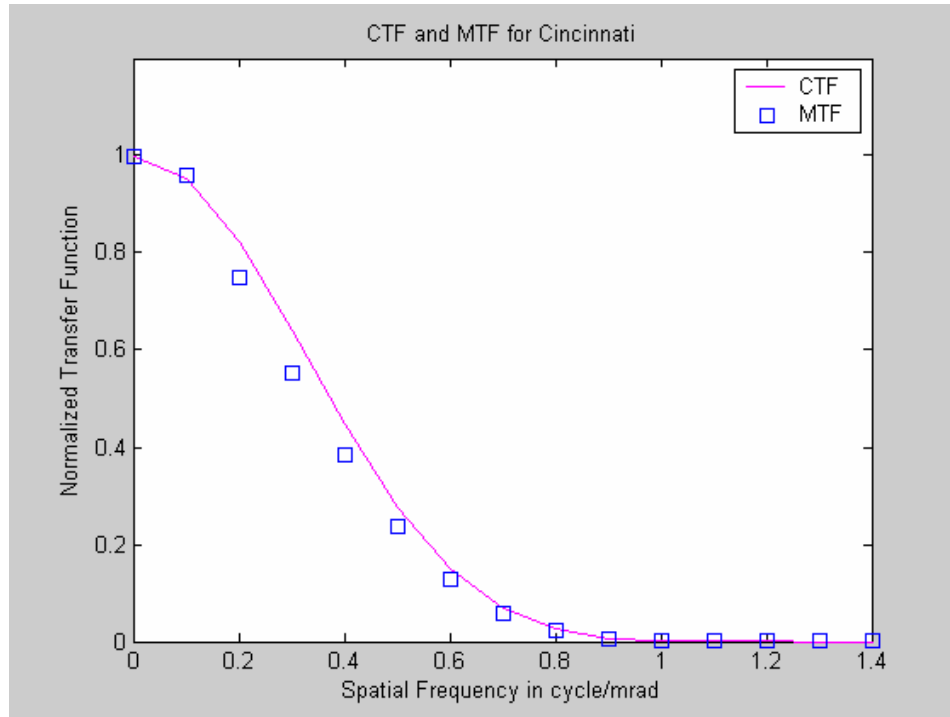


Figure 4.8 CTF and MTF plots for Cincinnati Thermal Imager.

The experimental values for Merlin thermal images are tabulated in Table 4.4. A similar sinc function was then used to curve fit the experimental CTF data. The cut off frequency is found iteratively to be 1.35 cycle/mrad from similar curve fitting. The curve fitting parameter, x , is found to be 1.3. Curve fitting of the CTF is shown in Figure 4.9 and plots of both CTF and MTF are shown in Figure 4.10.

F_s (cycle/mrad)	B_{\max} (mV)	B_{\min} (mV)	$B_{\max} - B_{\min}$ (mV)	$B_{\max} + B_{\min}$ (mV)	CTF	Normalized CTF
0.00	282	226	56	508	0.1102	1.0000
0.10	284	228	56	512	0.1094	0.9922
0.20	292	240	52	532	0.0977	0.8867
0.33	280	238	42	518	0.0811	0.7355
0.39	290	246	44	536	0.0821	0.7447
0.50	280	240	40	520	0.0769	0.6978
0.58	270	238	32	508	0.0630	0.5714
0.70	268	238	30	506	0.0593	0.5378
0.78	266	242	24	508	0.0472	0.4286
0.88	266	240	26	506	0.0514	0.4661

Table 4.4 CTF for Merlin thermal imager.

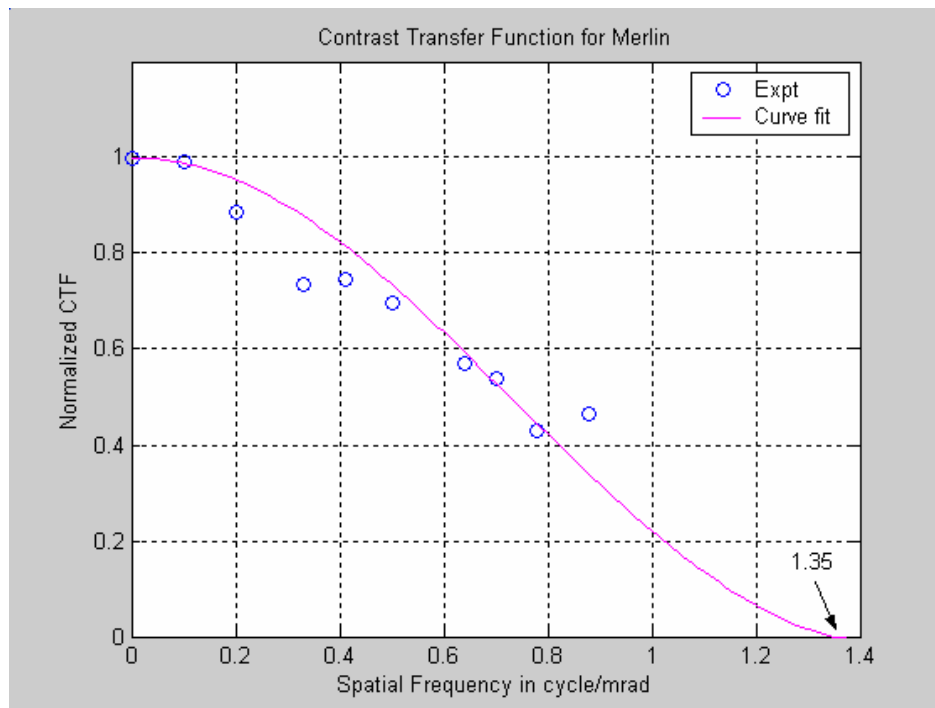


Figure 4.9 Plot of CTF result for Merlin thermal imager.

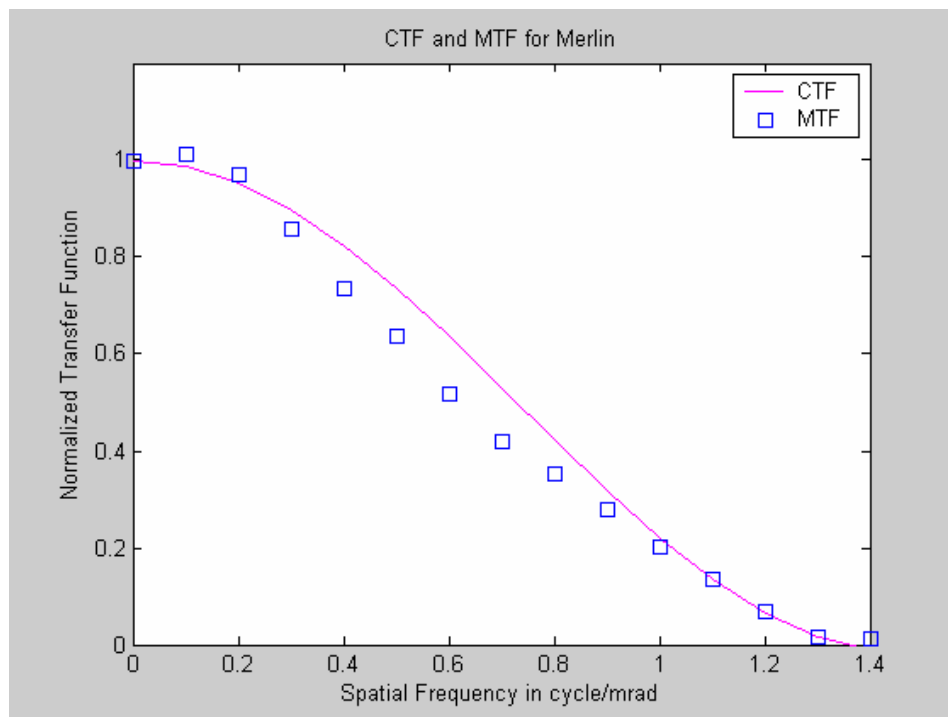


Figure 4.10 CTF and MTF plots for Merlin Thermal Imager.

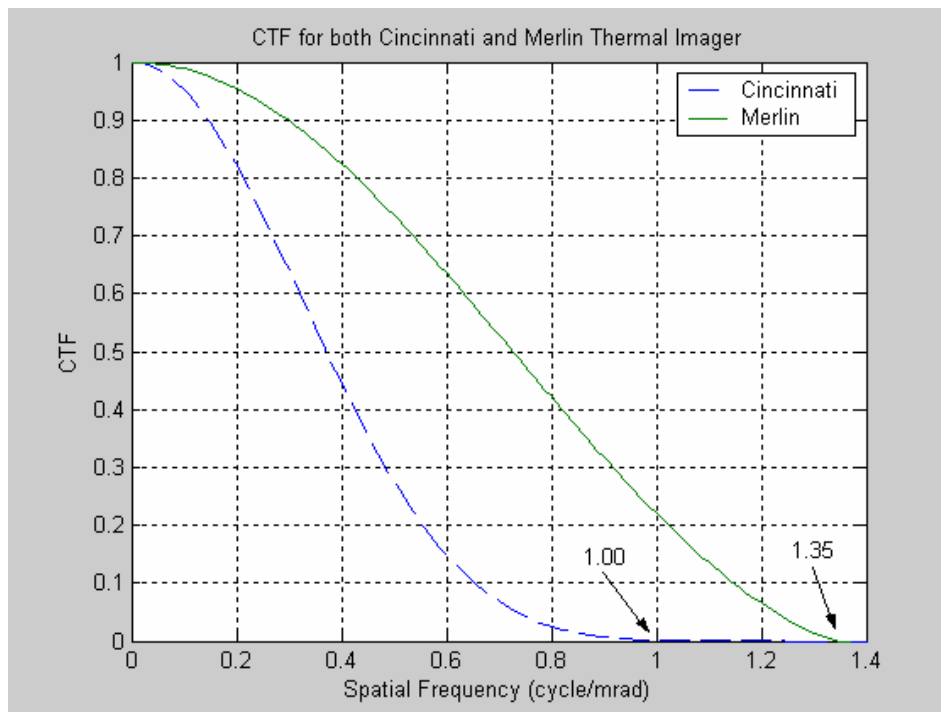


Figure 4.11 Comparison of CTF between Merlin and Cincinnati thermal imager.

The resolution limit of the imager is determined by the cut-off spatial frequency. Through the curve fitting process, the cut-off frequency of the Merlin is found to be approximately 1.35 cycle/mrad while that of Cincinnati is 1.00 cycle/mrad. The higher cut-off frequency of the Merlin camera implies that it can resolve smaller details than that of the Cincinnati imager.

Besides, the CTF of the Merlin thermal imager is found to be approximately twice or more than that of the Cincinnati at most spatial frequencies within the resolution limit. This can be clearly seen from the wide difference between the two plots in Figure 4.11. From the definition of CTF and MTF, this means that the Merlin thermal imager is more efficient in reproducing images as close to the actual objects for the same spatial frequencies.

3. Minimum Resolvable Temperature Difference

MRT results are tabulated in Table 4.5. Using equation (4.4), an appropriate curve was generated to best fit the data. The fitting parameter, A, was first determined to be approximately 0.05 by observing the temperature difference at the smallest spatial frequency. Using the least mean square optimization, B and C were found to be 0.1 and 3.9 respectively. From the plot (Figure 4.12), it can be estimated that the curve has an asymptote at a spatial frequency of about 1.18 cycle/rad. This corresponds to the cut-off frequency of the system.

F_s (cyc/mrad)	ΔT ($^{\circ}\text{C}$)
0.07	0.06
0.14	0.11
0.23	0.11
0.28	0.11
0.39	0.22
0.48	0.17
0.60	0.28
0.69	0.28
0.80	1.11

Table 4.5 MRT for Cincinnati thermal imager.

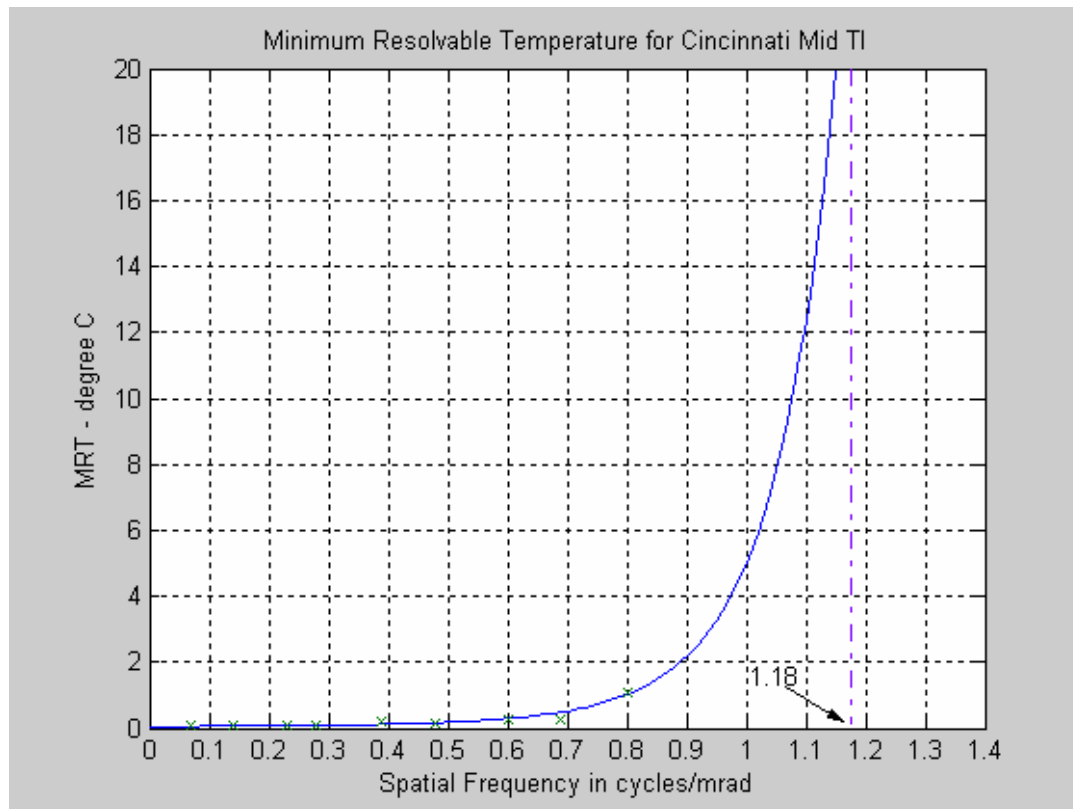


Figure 4.12 MRT plot for Cincinnati thermal imager.

Similar procedure and analysis were carried out for the Merlin thermal imager. The MRT result for the Merlin is presented in Table 4.6 and plotted in Figure 4.13. The curve is found to have the following curve fitting parameters.

$$A = 0.05$$

$$B = 0.1$$

$$C=3.8$$

F_s (cyc/mrad)	ΔT (°C)
0.10	0.11
0.20	0.17
0.33	0.17
0.39	0.22
0.50	0.28
0.58	0.33
0.70	0.44
0.78	0.83
0.88	1.33

Table 4.6 MRT for Merlin thermal imager.

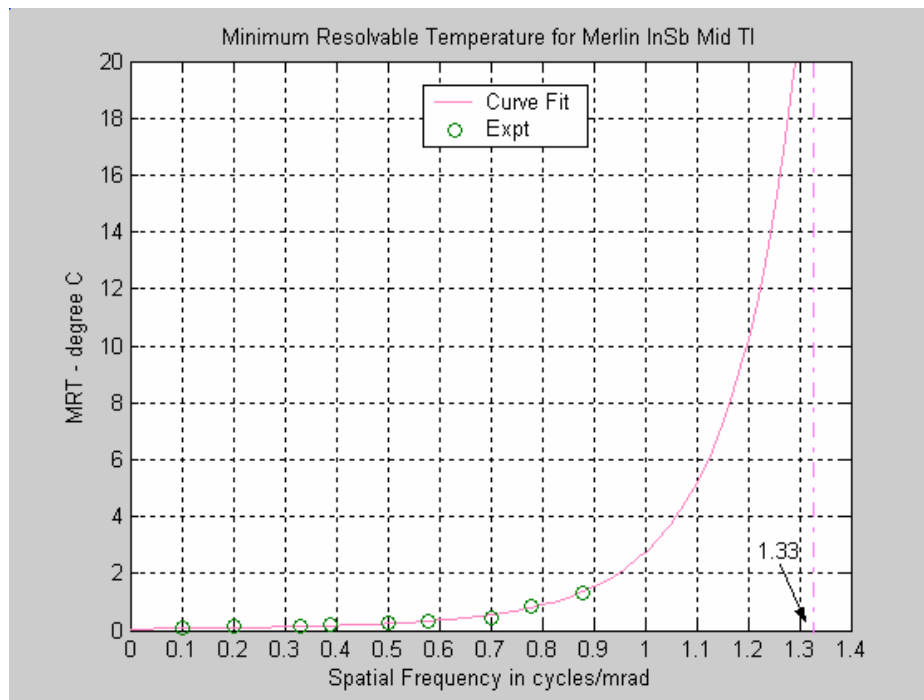


Figure 4.13 MRT plot for Merlin thermal imager.

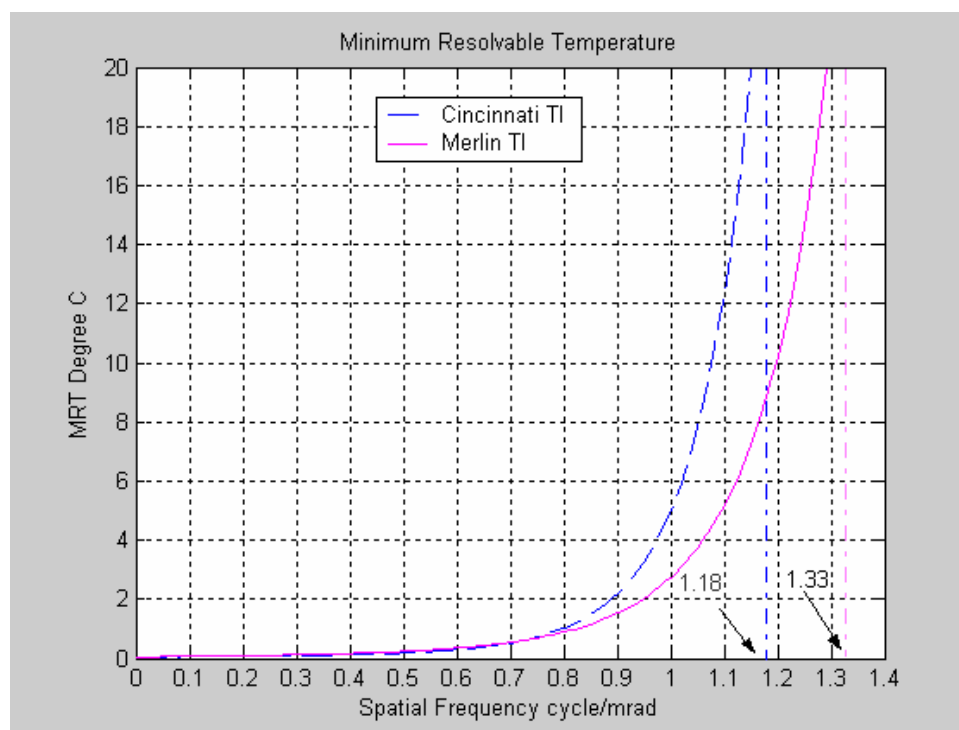


Figure 4.14 Comparison of MRT between Merlin and Cincinnati thermal imager.

The MRT plots (Figure 4.14) show that the cut-off frequencies for the Cincinnati and Merlin imagers are 1.18 cycle/mrad and 1.33 cycle/mrad respectively. This shows that the Merlin imager has a higher resolution limit than the Cincinnati imager. In addition, the cut-off frequency for the Cincinnati determined from the MRT measurement was higher than that found from the CTF experiments (1.18 cycle/mrad compared with 1.00 cycle/mrad), while the cut-off frequency for the Merlin is quite similar in both experiments. Theoretically, these figures should be the same based on equation (3.5); as the MTF tends to zero, MRT becomes asymptotic. The former discrepancy can be accounted for as due to the subjective nature of obtaining MRT experimentally. However, results are consistent in that the Merlin thermal imager can resolve smaller details than the Cincinnati thermal imager. Nonetheless, the two imagers are found to have similar sensitivity. These can be seen from their MRT values near to the lower spatial frequencies. From the experimental values for small spatial frequencies, the difference in temperatures for MRT values of both imagers averaged at about 0.1 °C.

Finally, as part of the acceptance test, this experimental MRT for the Merlin camera is compared with its theoretical MRT using equation (3.5). Using specifications from the manufacturer, together with the experimentally derived MTF values, the theoretical MRT is calculated and plotted using the parameters from Table 4.7. Both the graphs are plotted in Figure 4.15. It is seen that the experimental MRT does show similar cut-off frequency to the theoretical MRT; however, the theoretical MRT appears to have very good sensitivity across a wider range of spatial frequencies. Nonetheless, the plots are deemed to be in good agreement with each other considering the subjective nature of the experimental MRT and the fidelity of equation (3.5).

In conclusion, the Merlin is determined to have better resolution and dynamic range. Besides, it shows superior performance in reproducing smaller details across a wide range of spatial frequencies compared to the Cincinnati. This can be seen from the wide difference between the two CTF plots. The Merlin is, hence, recognized as desirable for use in follow-on research.

SNRT	1.0
v	From 0.01 to 1.4 cyc/mrad
MTF	From experimental MTF (Figure 4.10)
L	7
t_e (sec)	1×10^{-3}
F_r	30
N_{os}	1
N_{ss}	1
NET (K)	0.025 (K)
ρ_x	4
Δx (mrad)	2.609e-1
Δy (mrad)	2.609e-1

Table 4.7 Parameters used for theoretical MRT calculation (Equation 3.5)

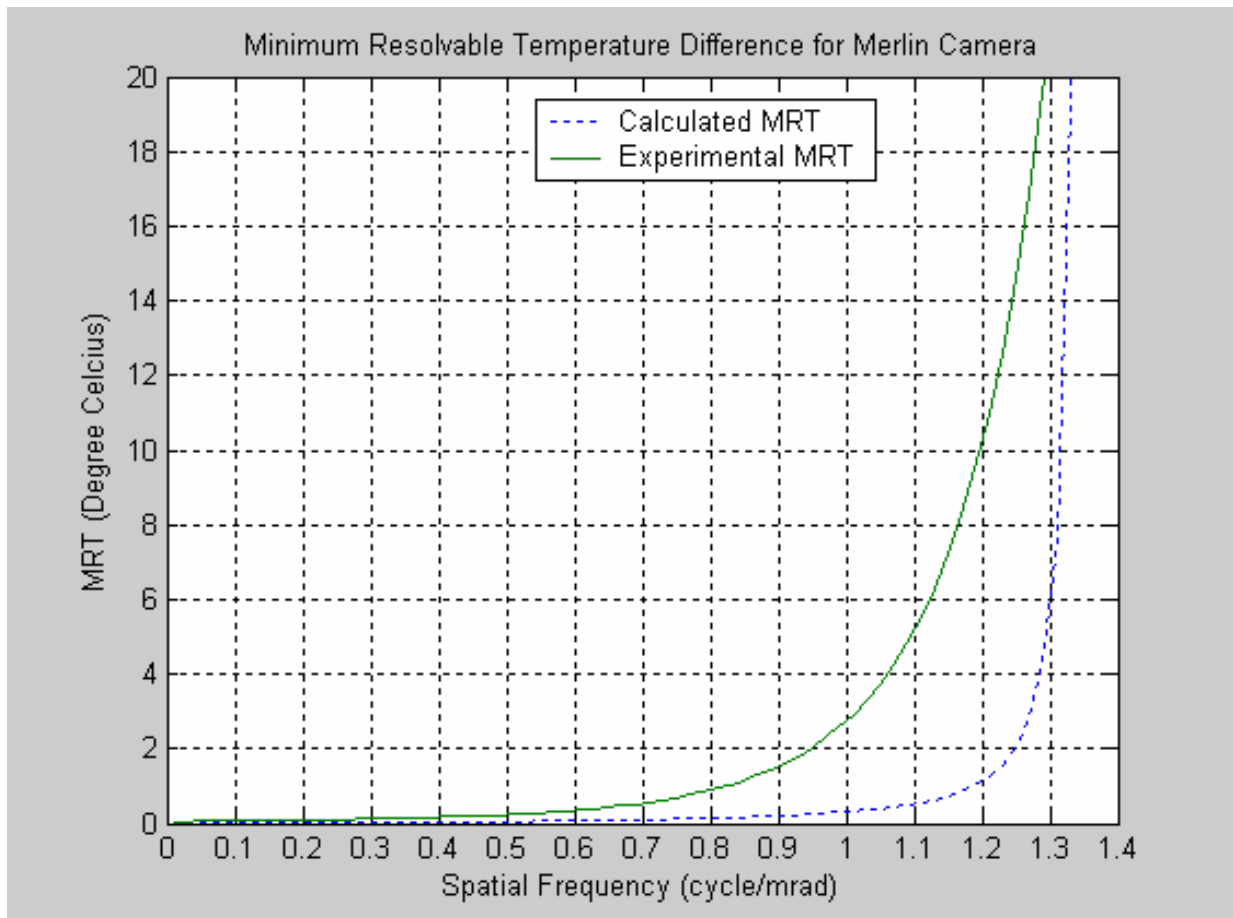


Figure 4.15 Comparison of calculated and experimental MRT.

V. SELECTION OF NARROW BAND FILTERS

The research objective of this thesis is to evaluate the possibility to discriminate the targets of interest from other thermal sources and background by correlating multi-narrow band images at the pixel level. This can be achieved by knowing the spectral response of the targets of interest and capturing their unique signatures using matching narrow band filters. Subsequently, this useful information can be correlated or fused together to better identify or discriminate targets. As a preliminary study, the spectral signature of fast moving air target is taken to be the target of interest and the appropriate narrow band filters within the MWIR are determined and purchased for this research.

A narrow band filter is used to gate a narrow unique spectral signature of the target of interest. The use of narrow band-width is expected to improve the SNR within its band since only the desired signal is captured exclusively. This assumes that the signature spectrum is narrower than the background. With the improvement of SNR within each narrow band filter output, correlating signal from various narrow bands is expected to better discriminate targets of interest from background or other deceptive infrared countermeasures

A. SPECTRAL BAND SELECTION

In selection of a spectral band in imaging system design, the determination of which spectral band maximizes the SNR depends on the spectral natures of the atmospheric transmission, of the optical transmission, and of the detector quantum efficiency. Dependence of noise on the spectral band is also of important consideration. However, Holst [9] explained that for staring systems, the noise can be considered as white over the regions of interest. Finally, in real application, the above mentioned factors are closely linked to the operating scenario and the targets of interest. For the purpose of this research, detection of aircraft and missile thermal signatures was chosen to be the area of

focus since thermal sensors are widely used in infrared missile seekers and search and track systems for the same purpose.

The two main contributors to missile and aircraft thermal signatures are their exhaust plume emission and airframe heating due to aerodynamic heating. Plume signature is due to the emission from large amounts of hot gases from combustion in the engines while aerodynamic heating is due to interaction between the target body surface and the atmosphere. This is very significant due to their high speeds compared to other sea or land platforms which are typically moving much more slowly. Many search and track IR sensor systems as well as IR missiles seekers make use of these observables as primary detection criteria. For the purpose of the investigation of improving SNR using narrow sub band filters, the filters selected were based on the spectrum of these two signatures.

B. EXHAUST PLUME SIGNATURE

The principal combustion products in the plume are carbon dioxide and water vapor, giving rise to characteristic molecular emission bands [16]. The strongest water bands are centered near 2.7 μm and 6.3 μm , whereas the strongest carbon dioxide band is centered near 4.3 μm with weaker bands at 2.7 μm and 15 μm . The spectral radiance between 4.2 μm and 4.5 μm is much larger than the water band at 2.7 μm . The so-called red and blue “spikes” at 4.0 μm are caused by absorption of the emission band by carbon dioxide in the atmosphere. Because of high temperature broadening, the plume radiation has significant amounts of shifted carbon dioxide radiation outside the absorption band that are transmitted. Figures 5.1 and 5.2 illustrate the formation of the blue and red spikes due to the overlap between the spectrum of the plume and the transmittance in the atmosphere. These two “spikes” offer a very distinct signature to distinguish the targets of interest from their background. The atmospheric transmittance is generated from MODTRAN for 20 °C, mid-latitude summer. One can also note that transmittance in the atmosphere decreases as range between target and sensor increases. This also corresponds to lower magnitude of the blue and red spikes as range increases, with greater attenuation of the red spike.

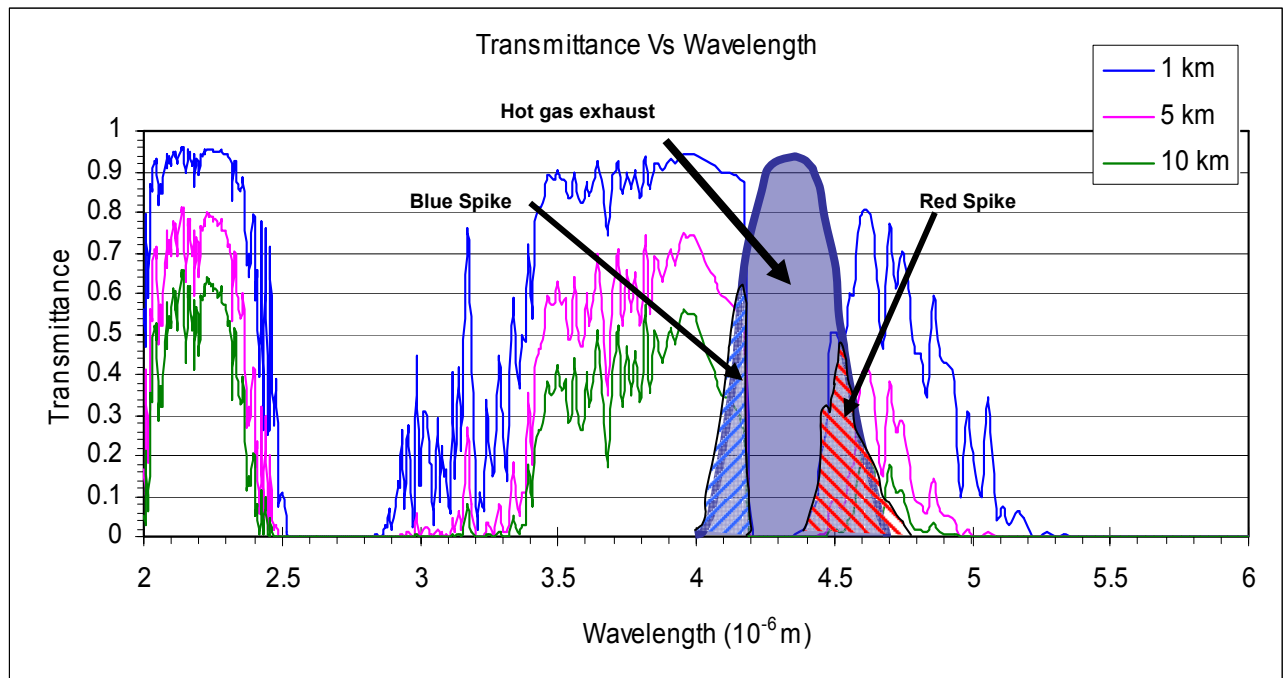


Figure 5.1 Superposition of an illustrative plume emission against the atmospheric transmission.

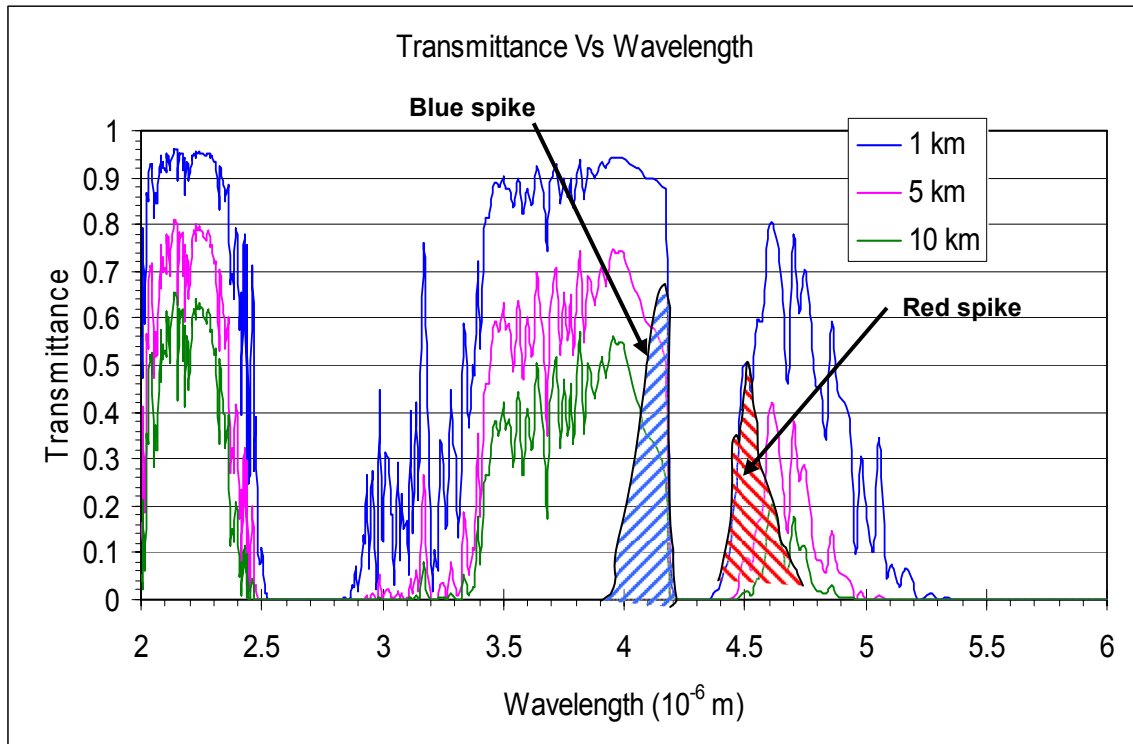


Figure 5.2 Formation of the blue and red spike in an aircraft exhaust plume signature as a result of atmospheric attenuation.

Figure 5.3 shows a typical structure of plume radiation at long range. Note that the radiation is viewed away from the tail aspect of an aircraft, part of which is obscured by the aircraft body, hiding the tail pipe grey body emission.

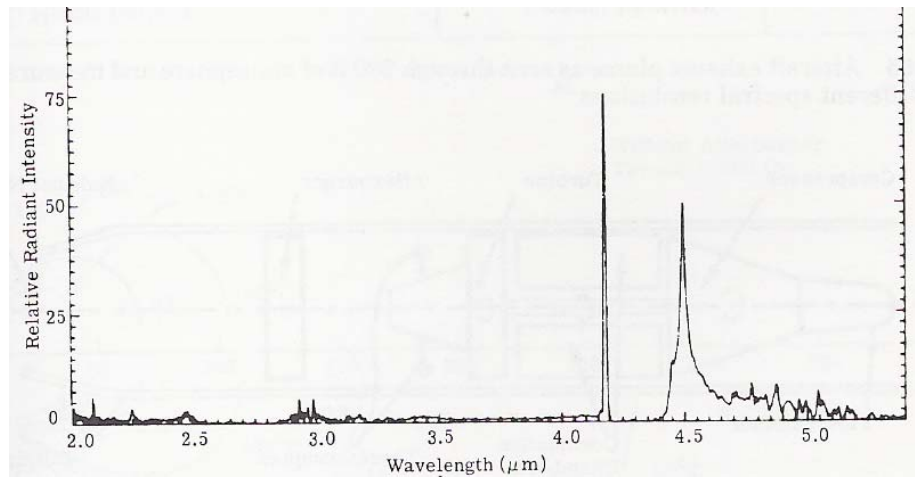


Figure 5.3 Relative spectrum of target exhaust plume emission when viewed away from the tail aspect. (From [17]).

C. AERODYNAMIC HEATING

Heating of a body can be experienced from rapid frictional interaction between two substances when in relative motion. As aircraft and missiles commonly travel at high speed through the atmosphere, the surfaces of these objects can be heated up dramatically, the effect known as aerodynamic heating. The extent of heating depends also on the materials interacting and the shape of the moving object.

The temperature of the skin increases as the speed of aircraft increases such that it is high enough to radiate. This radiation can become readily observable compared with other thermal signatures. Figure 5.4 shows the surface skin temperature as a function of Mach number for laminar flow over a surface above 37,000 ft of altitude [17].

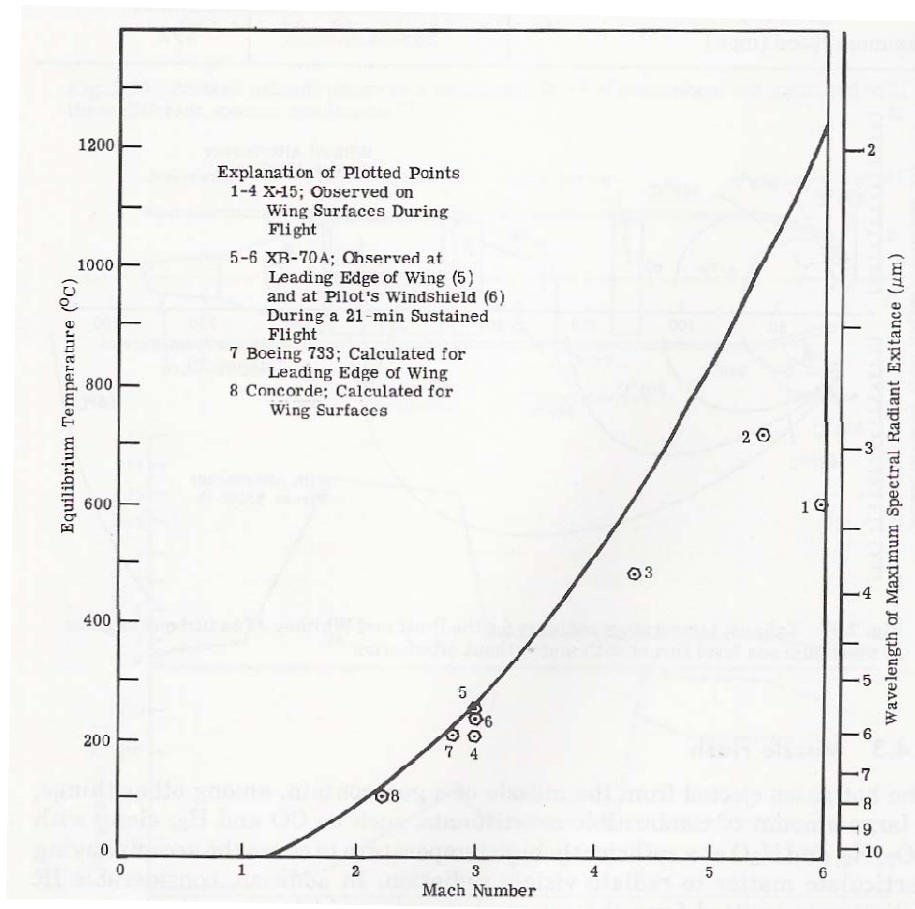


Figure 5.4 Equilibrium surface temperature caused by aerodynamic heating (for altitudes above 37,000 ft and laminar flow). (From [17]).

D. NARROW BAND FILTER SELECTION

As mentioned in the selection of high flying targets as our area of focus, it is worthwhile to look at a typical signature of an aircraft from other aspects. Figure 5.5 shows a good example of the spectral quality of aircraft radiation as observed from the tail aspect. Note that the plume signature is not significant relative to tailpipe emission when viewed from tail aspect because of the rapid decrease in plume temperature after leaving the tail pipe. The thermal signature from the tail aspect is, therefore, dominated by its tail pipe grey body emission and aerodynamic heating [19].

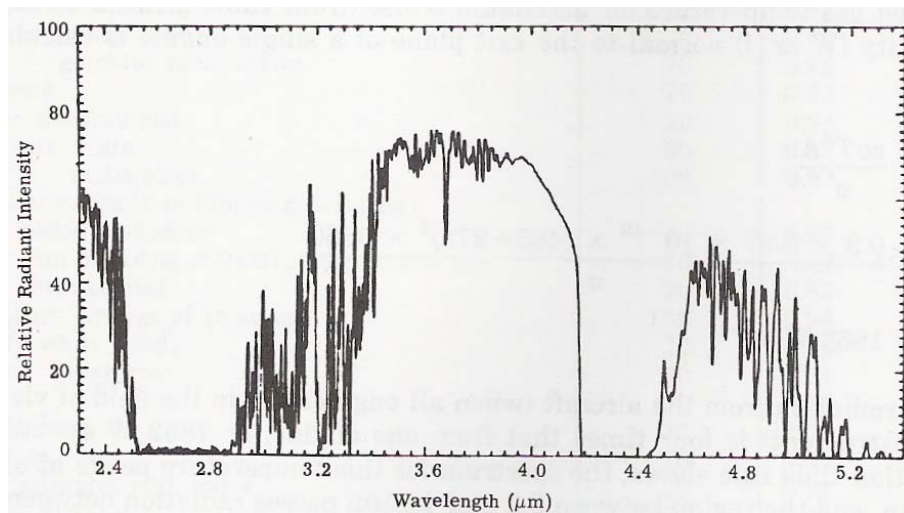


Figure 5.5 Relative spectrum of jet aircraft as seen from the tail aspect at a range of 1.5 miles. (From [17])

Knowing the typical aircraft radiation spectrum from various aspects, the desired filter bands were then selected. The filters used for this study were described in Table 5.1.

Figure 5.6 shows the passbands of the selected narrow bandpass filters with respect to the blue and red spikes. The exact widths for the filters were selected given the availability of filters from the manufacturer. These dimensions were deemed to be close to our requirements for this research purpose. Similarly, one narrow band filter was purchased to include a portion of signal due

to surface heating. (Figure 5.7) A sub-band that is nearer to 4.0 μm was selected because of the fact that this region attenuates less as range increases. This can be deduced from the atmospheric transmission plot of Figure 5.1.

Narrow Filter bands (nm)	Intended Spectral Signatures
3750/4020	Aerodynamic heating/ Tail pipe grey body emission
4540/4720	Red spike
4110/4720	Both blue and red spikes

Table 5.1 Narrow filter bands used in this study.

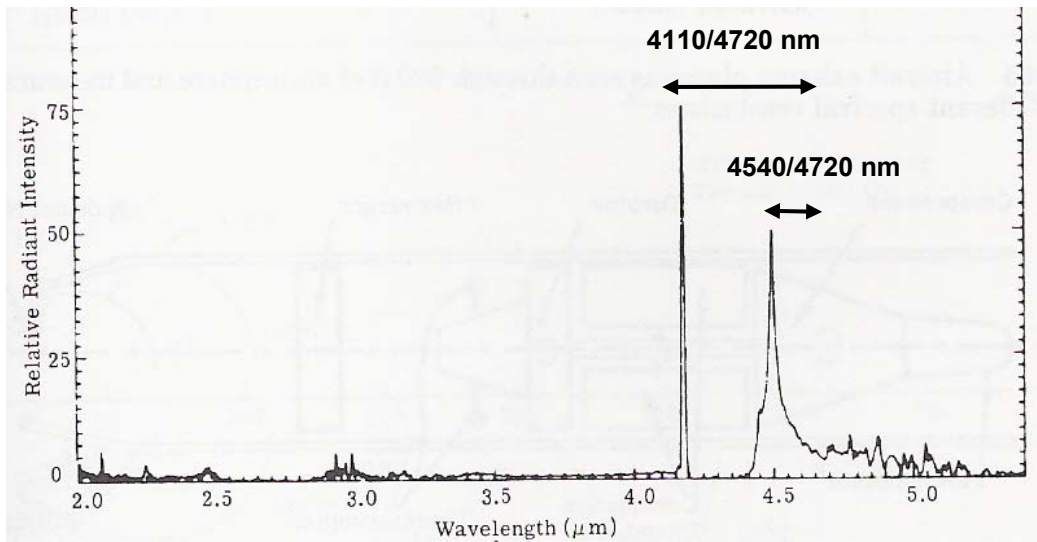


Figure 5.6 The selected narrow band filters bandwidths (arrows) compared to the blue and red spikes. (After [17])

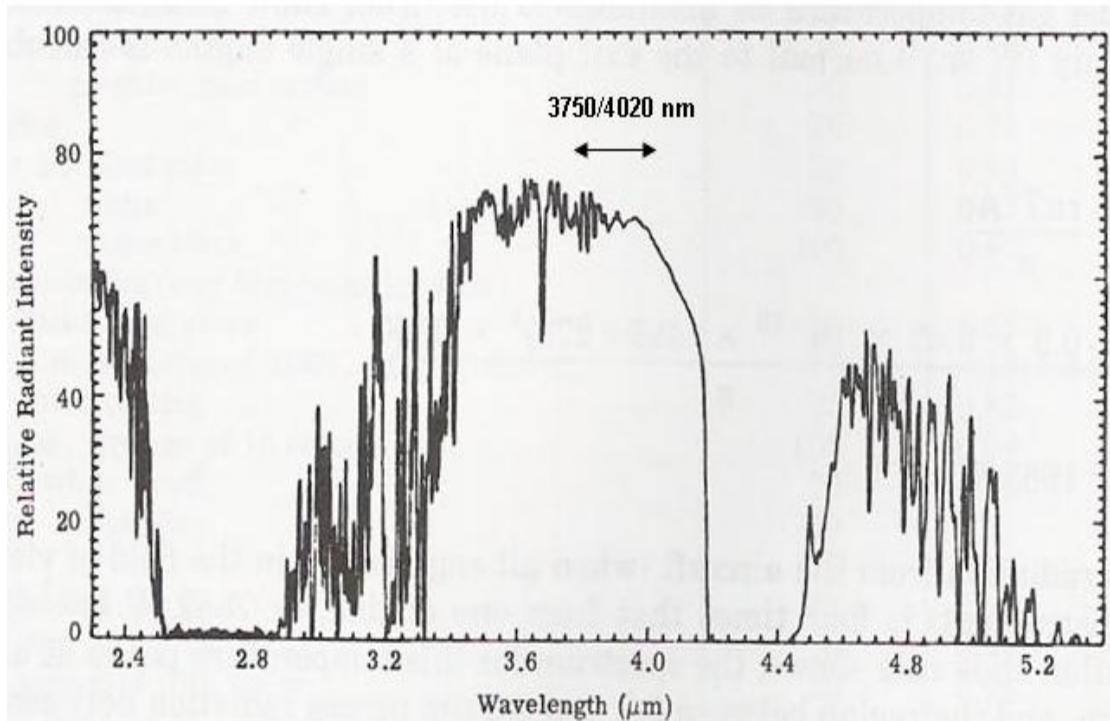


Figure 5.7 The selected narrow band filter (arrow) to include thermal signature mainly due to aerodynamic heating and tail pipe grey body emission. (After [17])

These selected filters were then installed in the Merlin Camera for further investigation of their performance (Chapter VI). The common parameters, CTF and MRT, were again used to characterize them. The images through these narrow filter bands were also collected and compared with those using the 3 to 5 μm filter. The comparison was carried out using the image acquisition software IRvista 2.51 provided by the Indigo System Corporation.

THIS PAGE INTENTIONALLY LEFT BLANK

VI. EXPERIMENTATION WITH NARROW BAND FILTERS

The selected narrow band filters were factory installed in the Merlin thermal imager by Indigo Systems Corporation. The thermal imager, with these narrow band filters, was then investigated for its new performance parameters as part of the characterization requirement. Finally, some images were acquired using the National Instrument (NI) frame grabber board, together with the Indigo IRvista 2.51 image acquisition software. These images were then used for comparisons with images in the 3 to 5 μm band, in terms of pixels intensity and other image characteristics.

The narrow band filters, IRvista, and the NI frame grabber board were installed and calibrated in-house by the Indigo Systems Corporation. The IRvista 2.52 is a real-time, image acquisition and analysis application that provides the user with acquisition, storage, retrieval, display, processing and analysis of still images and video in a Windows interface [18]. The National Instrument frame grabber board, PCI 1422 Card, is incorporated to acquire images and video. It is transparent to the user during operation. Bursts and live image streams can be saved to disk and later retrieved for analysis without loss of detail. A problem in compatibility between the Merlin imager and the IRvista program was found during initial installation. After some troubleshooting, it was found out with the assistance of Indigo Systems Corporation that a sub-program for IRvista, the IMAQ 2.6 from National Instruments, was not running properly with this hardware configuration setup. Specifically, the IMAQ 2.6 was not running well with Window XP Home edition. Subsequently, a newer version of IMAQ, IMAQ 3.0, was installed by Indigo¹.

¹The assistance of Dr. Richards Austin of Indigo Systems Corporation is gratefully acknowledged

The following table (Table 6.1) shows the configuration of the cold filter wheel in the imager, the associated Non-Uniformity Correction (NUC) table and their integration time upon calibration. Note that the integration time is set to be longer for the narrow filters for satisfactory image acquisition. The filter responses of all the filter bands are given in Appendix B

Filter Wheel Position	Narrow Band Filter (nm)	NUC	Integration Time (μ s)
1	3750/4020	2	16000
2	4540/4720	3	8000
3	3000/5000	0	2600
4	4110/4720	1	5000

Table 6.1 Details of calibrated Merlin Camera with narrow band filters.

A. CONTRAST TRANSFER FUNCTION

The same experimental procedure, as described in Chapter IV, section B2, was used to investigate the CTF of the narrow band filters. The experimental CTF results for all three filter bands are shown in Tables 6.2 to 6.4. These results are also plotted and presented in Figure 6.1 for ease of comparison. Table 6.5 gives all the values of the curve-fitting parameter x as defined in equation (4.1).

F_s (cycle/mrad)	B_{max} (mV)	B_{min} (mV)	B_{max} - B_{min} (mV)	B_{max} + B_{min} (mV)	CTF	Normalized CTF
0.00	240	184	56	424	0.1321	1.000
0.07	238	184	54	422	0.1280	0.969
0.14	260	206	54	466	0.1159	0.877
0.23	264	210	54	474	0.1139	0.863
0.27	250	210	40	460	0.0870	0.658
0.35	250	212	38	462	0.0823	0.623
0.41	246	212	34	458	0.0742	0.562

Table 6.2 CTF values for filter band 4110/4720 nm

F_s (cycle/mrad)	B_{max} (mV)	B_{min} (mV)	B_{max} - B_{min} (mV)	B_{max} + B_{min} (mV)	CTF	Normalized CTF
0.00	220	184	36	404	0.0891	1.000
0.07	218	184	34	402	0.0846	0.949
0.14	226	198	28	424	0.0660	0.741
0.23	230	200	30	430	0.0698	0.783
0.27	226	200	26	426	0.0610	0.685
0.35	226	202	24	428	0.0561	0.629
0.41	218	200	18	418	0.0431	0.483

Table 6.3 CTF values for filter band 3750/4020 nm

F_s (cycle/mrad)	B_{\max} (mV)	B_{\min} (mV)	$B_{\max} - B_{\min}$ (mV)	$B_{\max} + B_{\min}$ (mV)	CTF	Normalized CTF
0.00	232	184	48	416	0.1154	1.000
0.07	228	182	46	410	0.1122	0.972
0.14	250	204	46	454	0.1013	0.878
0.23	256	210	46	466	0.0987	0.856
0.27	242	208	34	450	0.0756	0.655
0.35	246	214	32	460	0.0696	0.603
0.41	244	214	30	458	0.0655	0.568

Table 6.4 CTF values for filter band 4540/4720 nm

Band filter (nm)	x parameter
4110/4720	4.222
3750/4020	4.906
4540/4720	4.308

Table 6.5 Curve fitting parameter x for CTF of various color filters as defined in equation (4.1).

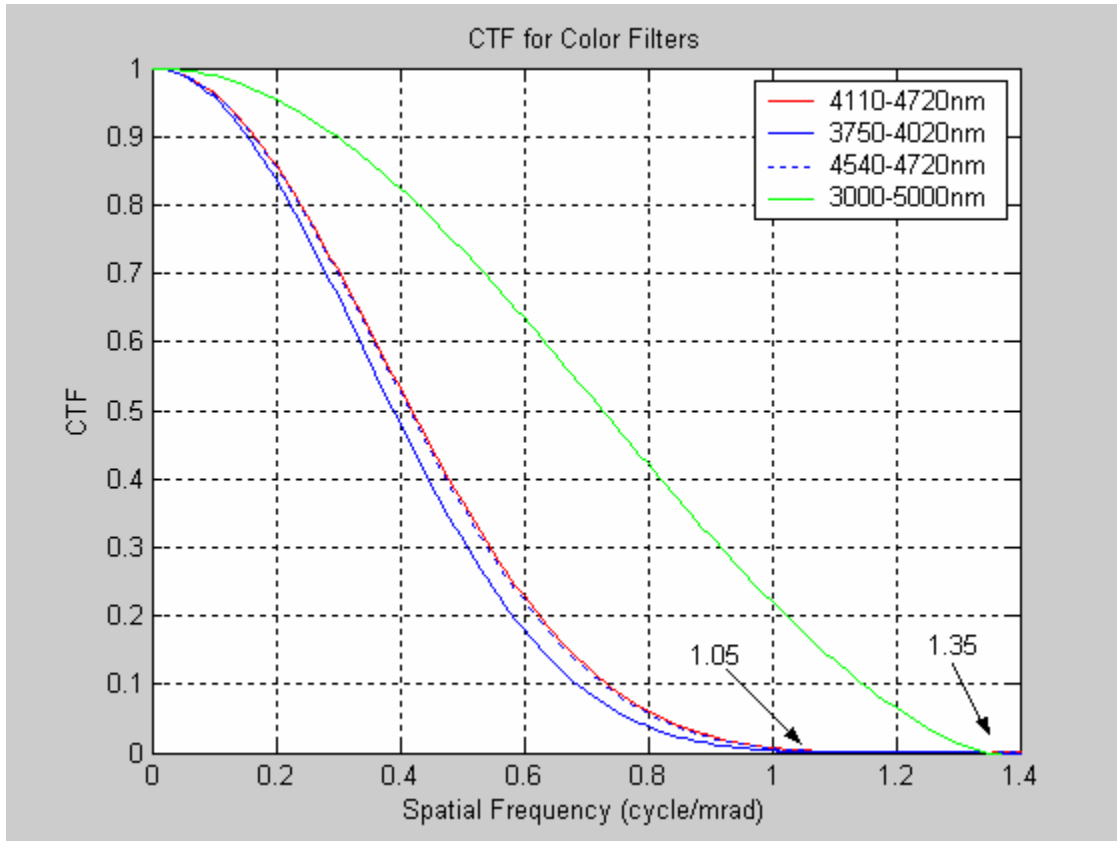


Figure 6.1 CTF of all the various filter bands

Based on the above plots, the CTFs for narrow band filters are found to be much lower than that of the 3000/5000 nm filter. Besides, the cut-off frequency for the narrow band filter is lower (1.05 cycle/mrad) compared with that of the full mid-wave spectrum (1.35 cycle/mrad). This means that the sensor with narrow band filters cannot resolve as fine target detail as with the latter. It can be seen from Tables 6.2 to 6.4 that the available experimental spatial frequencies are quite low, below 0.5 cycle/mrad. The 4 bar scan signal could not be resolved on the oscilloscope screen at higher frequencies. The rest of the CTF curve is generated using a matching sinc function based on these low frequency points. It could be suggested that this degradation in performance is due to low levels of radiant energy transmitted through the narrow band filter. However, Holst [9] has pointed out that MTF does not contain any signal intensity information. It is interpreted rather that this experimental setup is system noise limited, as a direct

result of the lower radiant energy from the target source compared to existing noise in the whole system. Although there may be no direct relationship between MTF and radiant energy, the lower target signal could not be discerned due to low signal to noise ratio.

It is worthwhile to reiterate that the source (bar target) represents blackbody radiation near room temperature. The radiance is low at mid wave frequencies and peaks at 10 μm at 300K. (Figure 2.2). Measurement temperature difference is in the proximity of 1 K.

B. MINIMUM RESOLVABLE TEMPERATURE DIFFERENCE

The MRT of the camera with various filters was measured using the same procedure as in Chapter IV, Section B3. The results are tabulated in Tables 6.6 to 6.8. These values are also plotted in Figure 6.2 for ease of comparison using the Hepfer technique described in Chapter IV. Table 6.9 shows the curve fitting parameters as defined in equation (4.4). The parameter A was again determined through observation of the MRT values at low spatial frequencies. This gives a direct measure of the sensitivity of the system. The 4110/4720 nm band filter is seen to allow better sensitivity compared to the rest. It shows similar sensitivity to the 3000/5000 nm filter band, although the latter could show better sensitivity due to its broader spectrum. This could be due to the experimental limitation imposed by the sensitivity of the thermocouples indicating the front and back plate temperatures.

F_s (cyc/mrad)	ΔT (°C)
0.07	0.11
0.14	0.11
0.23	0.17
0.27	0.17
0.35	0.22
0.41	0.22
0.58	0.83

Table 6.6 MRT values for filter band 4110/4720 nm.

F_s (cyc/mrad)	ΔT (°C)
0.07	0.17
0.14	0.17
0.23	0.22
0.27	0.17
0.35	0.22
0.41	0.28
0.58	0.89

Table 6.7 MRT values for filter band 3750/4020 nm.

F_s (cyc/mrad)	ΔT (°C)
0.07	0.22
0.14	0.22
0.23	0.28
0.27	0.22
0.35	0.28
0.41	0.28
0.58	1.00

Table 6.8 MRT values for filter band 4540/4720 nm.

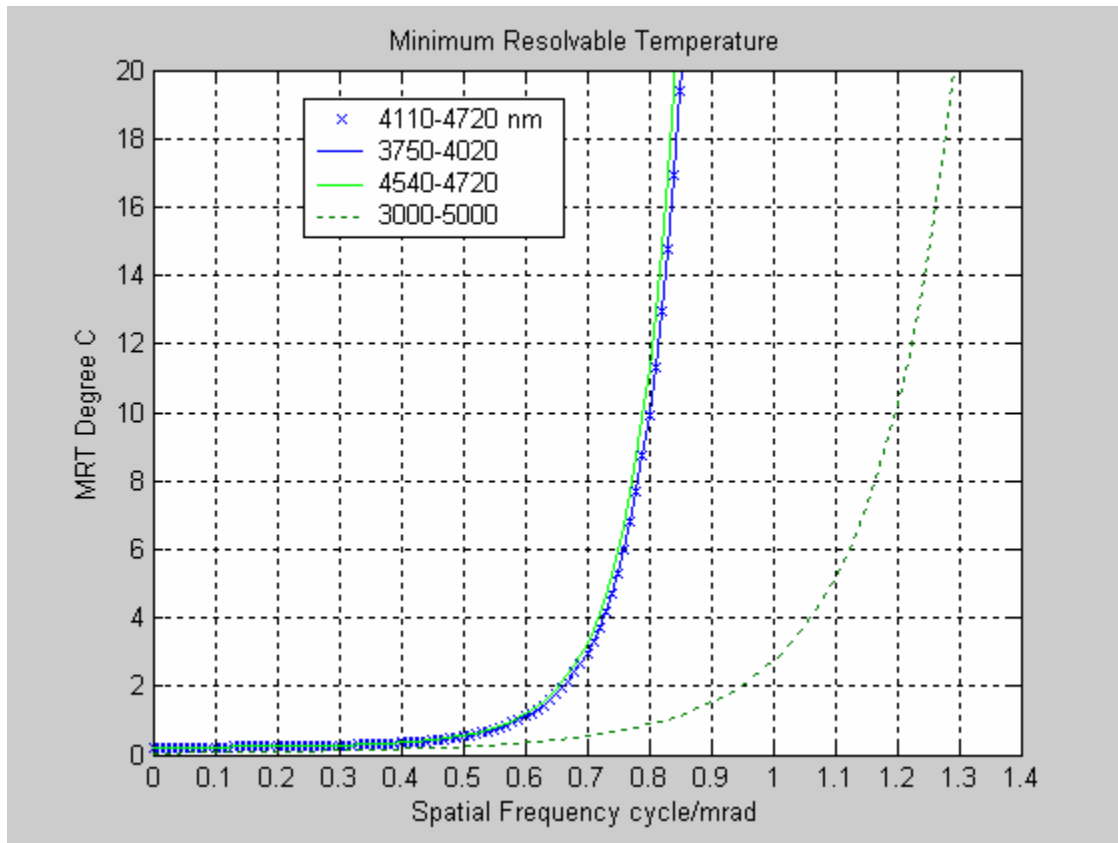


Figure 6.2 MRT of all the various filter bands

Band filter (nm)	A	B	C
4110/4720	0.11	0.1	7.5
3750/4020	0.17	0.1	7.5
4540/4720	0.22	0.1	7.7

Table 6.9 Curve fitting parameters A, B and C of MRT for various band filters as defined in equation (4.4)

The MRT response for the 3000/5000 nm filter band lies to the right of the narrow band filters. Narrow band filters are, hence, found to have smaller cut-off

frequency (0.9 cycle/mrad) compared to that for 3000/5000 nm filter (1.33 cycle/mrad). This narrow band cut-off frequency is also close to that obtained from the CTF values. Generally, the MRT results are in agreement with measurements of CTF. The broader band filter gives better performance compared to each individual narrow band filter in terms of resolution and sensitivity. It is concluded that lower radiant energy in the case of narrow bands dominates the cause for such observation. In accordance with the CTF experiment, the narrow band filters are apparently operating in a system noise-limited environment.

C. ANALYSIS OF NARROW BAND IMAGES

Having investigated the characteristics of narrow band filters, images of a propane flame were acquired, using the IRvista 2.51 software, to verify their potential to improve imaging and target discrimination. This was done for all three narrow bands and the 3000/5000 nm band. The images were then analyzed and compared using pixel number and pixel intensities.

1. Experimental Procedures

Once the performance characteristics of these narrow band filters were known, images of a real thermal source were acquired for further analysis. A lighted propane burner was used as a heat source in a laboratory setting. The imager was placed about 1.5 m from the burner. Figure 6.3 shows the view that was acquired by the thermal imager. The filter wheel of the imager was first adjusted to the desired filter band before image acquisition. The image was then captured using the IRvista interface. Two analysis tools, the image area statistical tool and image intensity windowing, were primarily used to analyze the images acquired. This procedure was subsequently repeated for the various filter bands.

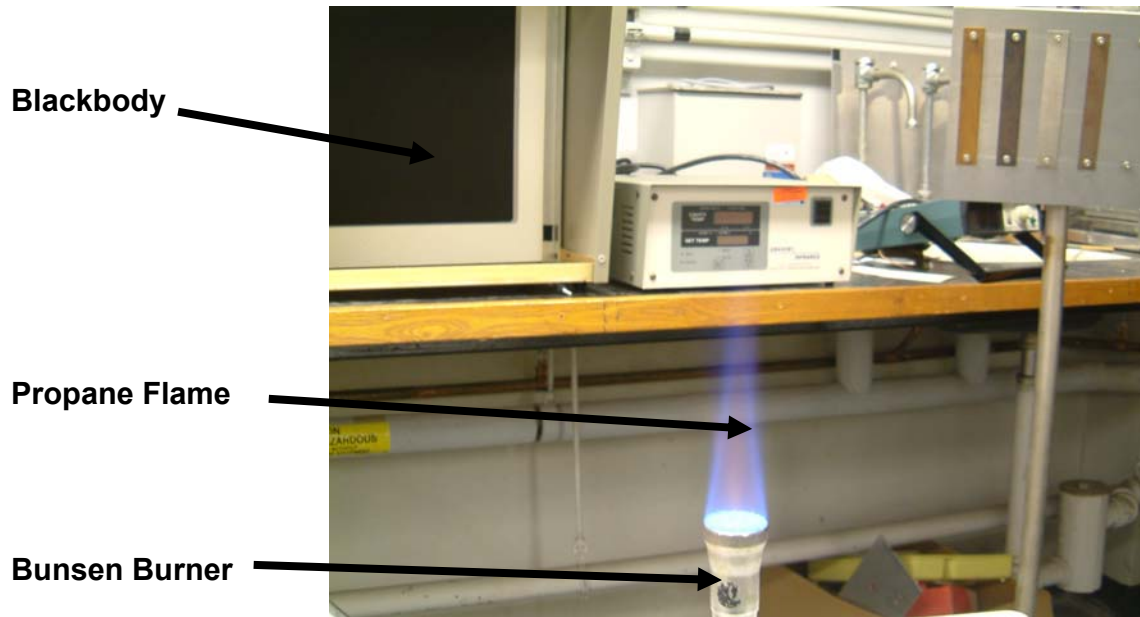


Figure 6.3 Visual image of scene to be acquired by the thermal imager.

It is important to know the thermal spectrum of a typical hydrocarbon flame in order to carry out meaningful analysis. Figure 6.4 shows an infrared emission spectrum of a Bunsen flame burning natural gas. This spectrum is published by Hudson [19] who observes that the spectra of many different types of flame are similar; all show a strong emission band between 4 and 5 μm . The emission is dominated by the combustion products of the hydrocarbon, namely the CO_2 and H_2O , both formed at elevated temperature. The spectral distribution of the Bunsen burner propane flame is similar to the actual exhaust plumes of rockets engines as shown in Figure 6.5. This strong emission band corresponds to the CO_2 emission peak at 4.3 μm wavelength. The signature of this emission band is significant at close proximity to the source as there is negligible absorption by atmospheric molecules. It is expected that the imager will detect the high radiant energy of this CO_2 emission. Given the filters used, only the 3000/5000 nm and 4110/4720 nm filters encompass the CO_2 emission peak., while the 3750/4020 nm filter does not cover this peak at all. The 4540/4720 nm band filter may capture part of this emission because the emission band

broadens and shifts toward shorter wavelengths due to higher temperature and pressure in a flame.

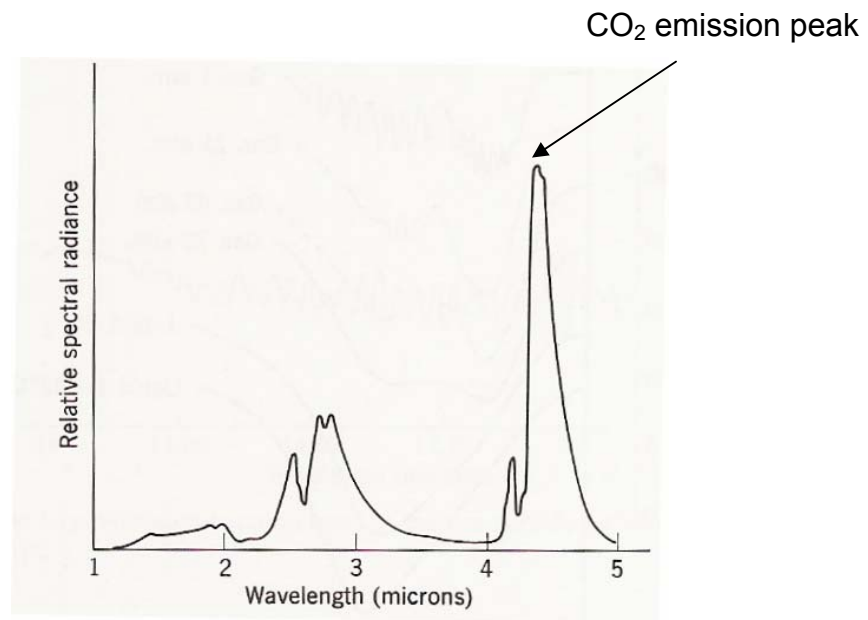


Figure 6.4 Infrared emission from a Bunsen flame burning natural gas. (From [19])

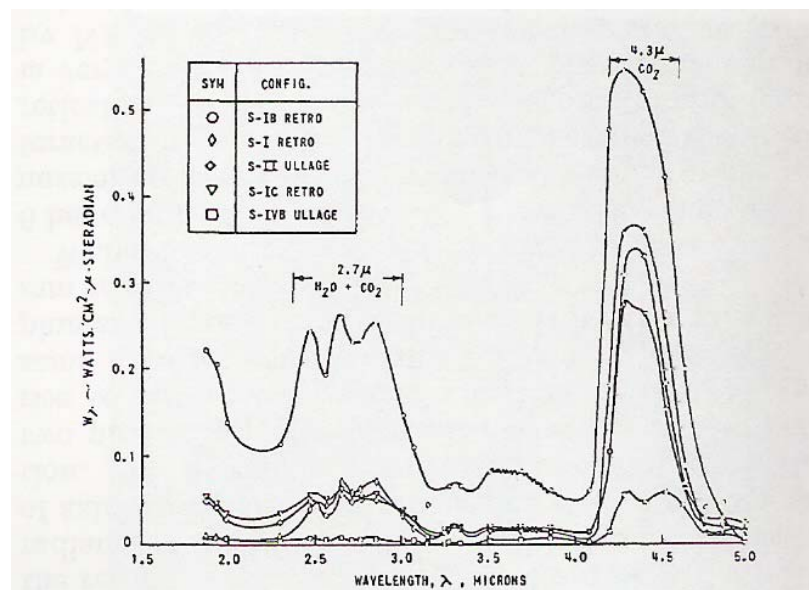


Figure 6.5 Exhaust plume radiance as a function of wavelength for five solid propellant engines. From [21]

2. Image Intensity Windowing Statistical Analysis

The Image Intensity Windowing Statistical tool provided in IRvista allows one to determine statistically the intensity of the captured or live images in terms of pixel number and pixel values. The statistics are presented in histogram form with the x axis as pixel value and y axis pixel number. This means that the area under the distribution gives the total number of pixels. For a 12-bit image, all the pixels in the image are scaled to give a value within 4096 possible values of intensity or pixel values. The detailed operation of this statistical tool is given in Appendix C.

Figure 6.6 and 6.7 show the same scene, as depicted in Figure 6.3, acquired using the IRvista interface and the corresponding image intensity windowing histograms. Note that with these grey color scale images, objects at higher temperature appear whiter while those at lower temperature appear darker.

The following observations are made. The image intensity generally peaks at pixel values of about 2000, 3900 and 4100 for all filters except for 3750/4020 nm filter. By comparing the hot spots and the total image area, it is deduced that the peaks at 3900 and 4100 pixel intensity correspond to both the propane flame and 'bright' background radiation, and 2000 pixel intensity corresponds to the uniform background intensity. The 'bright' background spot is identified as that of laboratory blackbody equipment which is about 1 m away. The blackbody has absorbed heat from the flame and re-radiated the thermal energy. There could have been reflection from its metal casing as well. It is further observed that the peak at 4100 is absent for the 3750/4020 nm filter and is low for the 4540/4720 nm filter. This observation further concludes the presence of the CO₂ emission peak.

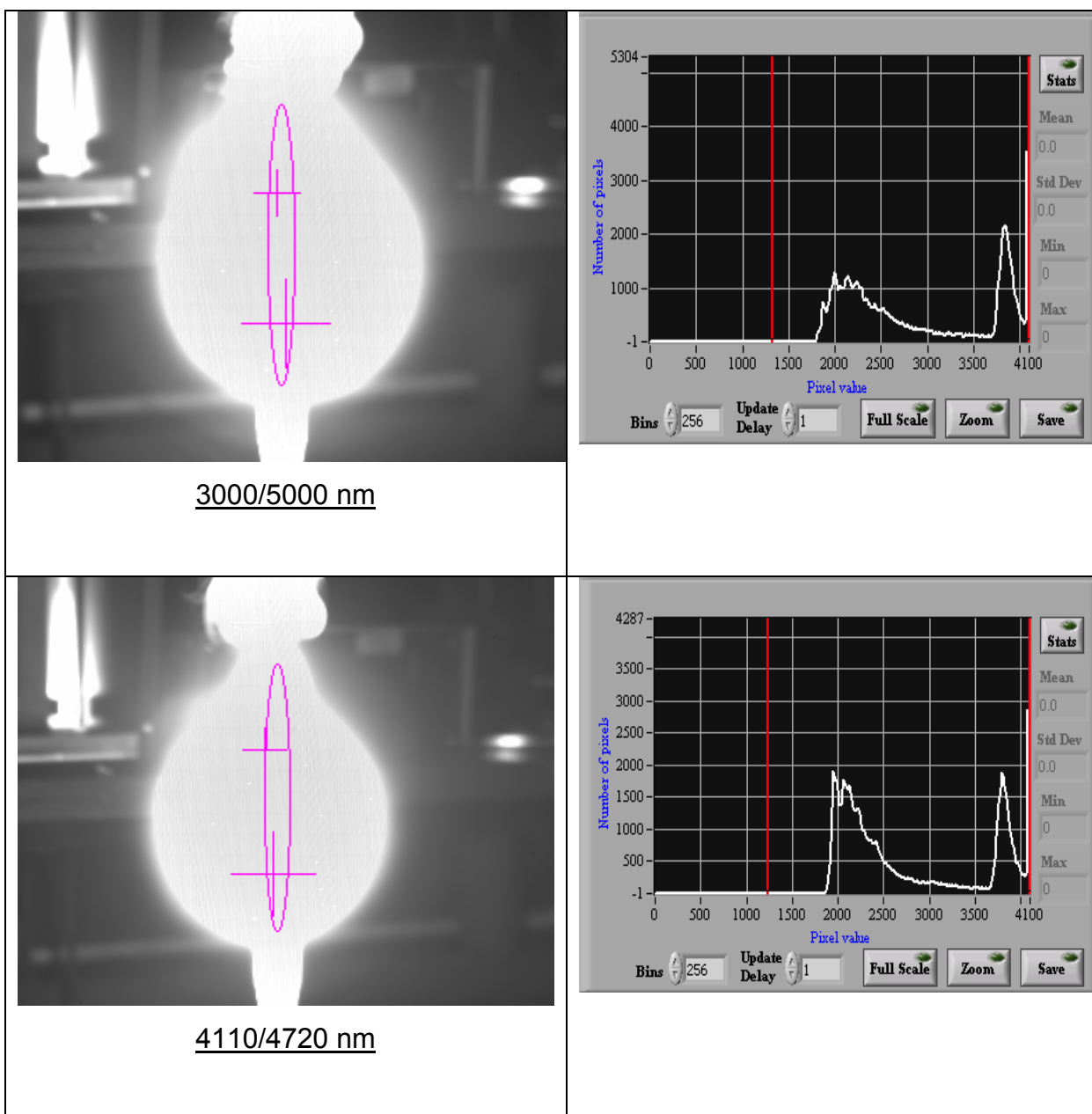


Figure 6.6 Images of the propane flame acquired using IRvista interface for 3000/5000 nm and 4110/4720 nm filter bands and the corresponding image intensity histograms.

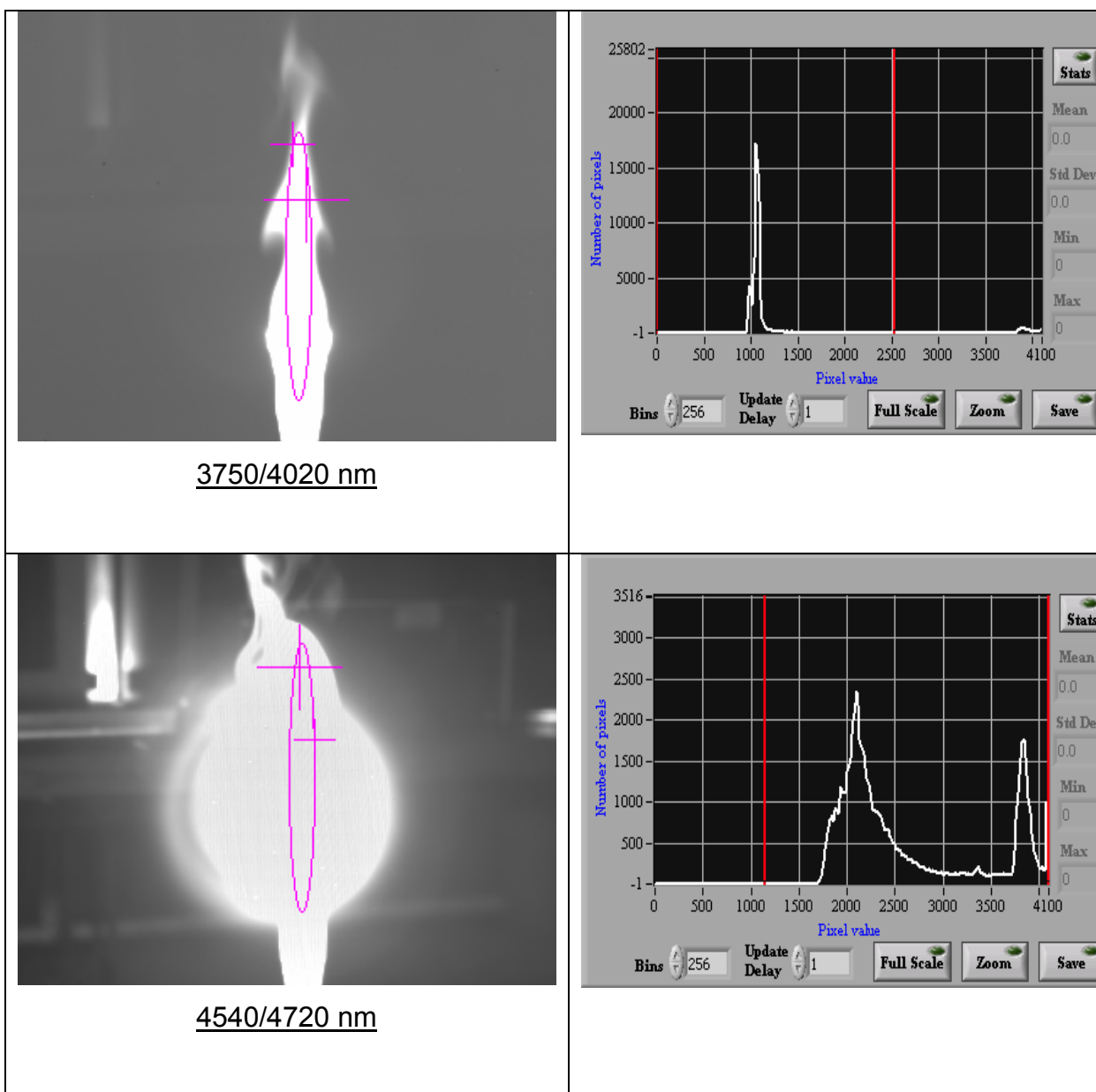


Figure 6.7 Images of the propane flame acquired using IRvista interface for 3750/4020 nm and 4540/4720 nm filter bands and the corresponding image intensity histograms.

The image corresponding to the 3750/4020 nm filter appears significantly different from the other three images. The flame image appears as a narrow elliptical hot spot with the rest of the surroundings having uniform temperature. In the histogram, there are two peaks. One peaks at about 1000 pixel intensity, the other peaks at about 3900 pixel intensity. The peak at the 1000 pixel intensity is deduced to correspond to the background given its proportionality and that of the 3900 pixel intensity reflects the narrow hot spot. Further experimentation shows that this outcome is due to the effect of the Automatic Gain Control (AGC) function. Due to high integration time (16000 μ s) for this band, the AGC scales the intensity downwards. (The integration time was calibrated using blackbody radiation at room temperature). This results in the observed image and its statistical behavior. Nonetheless, this image seems to be better in discriminating the target of interest from the background compared to the other three filters just by having AGC to wash out the lower thermal source. However, this method is not sufficiently reliable for use in discriminating targets of interest.

The idea of discriminating targets is further elaborated using Table 6.10. In Table 6.10 (b), the ratio of pixel number at two main peaks to the pixel number of background is tabulated. This table essentially gives the unique signature of propane emission at close proximity for various bands. A blackbody radiating at 1000K will have a table typically showing high pixel values across all the narrow filter bands, as can be deduced from Figure 2.2. It will not have higher peak radiance at 4.3 μ m (4100 pixel value) as in the case for a hydrocarbon flame. A simple algorithm can be established to distinguish this table from that of a blackbody easily. Similarly, this concept can be extended to discriminate other thermal sources in the environment such as solar radiation. Figure 6.8 shows the graphical representation of the data tabulated in Table 6.10.

Sources of Radiation	Peak Pixel Values	No. of Pixels corresponding to different radiant sources for each filter band			
		3000/5000	4110/4720	3750/4020	4450/4720
Background	*1000 or 2000	1200	1900	17000	2800
Flame	3900	2200	1900	1000	1700
CO ₂ emission	4100	3500	2800	-	1000

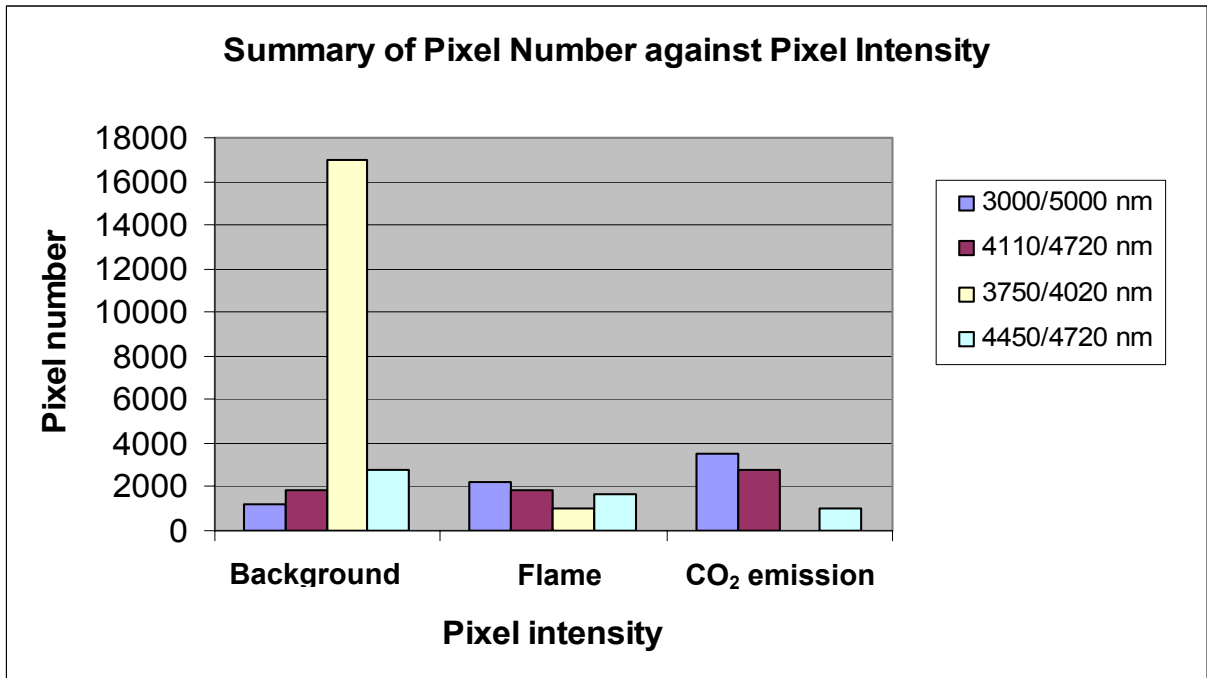
(a)

Sources of Radiation	Peak Pixel Values	Normalized No. of Pixels corresponding to different radiant sources for each filter band			
		3000/5000	4110/4720	3750/4020	4450/4720
Background	*1000 or 2000	1.00	1.00	1.00	1.00
Flame	3900	1.83	1.00	0.059	0.61
CO ₂ emission	4100	2.92	1.47	-	0.36

(b)

Table 6.10 The number of pixels corresponding to various peak pixel values from Figure 6.6 and 6.7. (a) Raw data (b) Normalized against background pixel number.

* For filter 3750/4020 nm, the pixel value of 1000 corresponds to background radiance while a pixel value of 2000 corresponds to background radiance for all other filters. These pixel values are scaled values as discussed in the text.



(a)

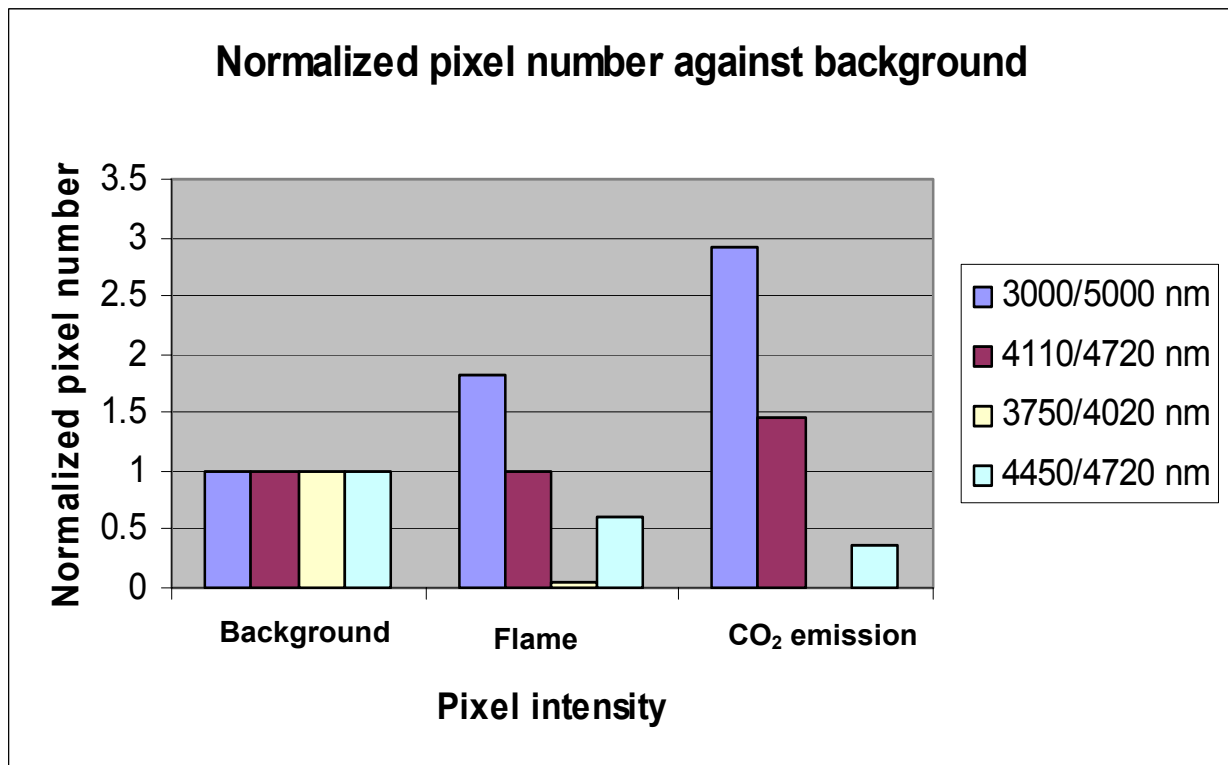


Figure 6.8 In graphical form, the number of pixels corresponding to various peak pixel values from Figure 6.6 and 6.7. (a) Raw data (b) Normalized against background pixel number

3. Image Area Statistical Analysis

The Image area statistical tool was also used for analyzing the intensity statistics of the images acquired. This tool allows image statistics to be displayed for the entire image or a region of interest (ROI). The tool can be used to calculate and display the mean, standard deviation, minimum and maximum of selected portion of an image in terms of pixel intensity values. The positions of minimum and maximum intensity can also be displayed readily. One can choose from a rectangular region of interest or an elliptical ROI.

In this analysis, an elliptical ROI was used as it was deemed to be more suitable to represent the area of interest of a burning flame as shown (Figure 6.9). There are two cross hairs shown within the ROI. The larger cross hair indicates the maximum intensity while the smaller one represents the minimum point within the ROI. The statistical values, in terms of pixel values, within the elliptical ROI are also given below each image in the figure. The same elliptical ROI is used for all images.

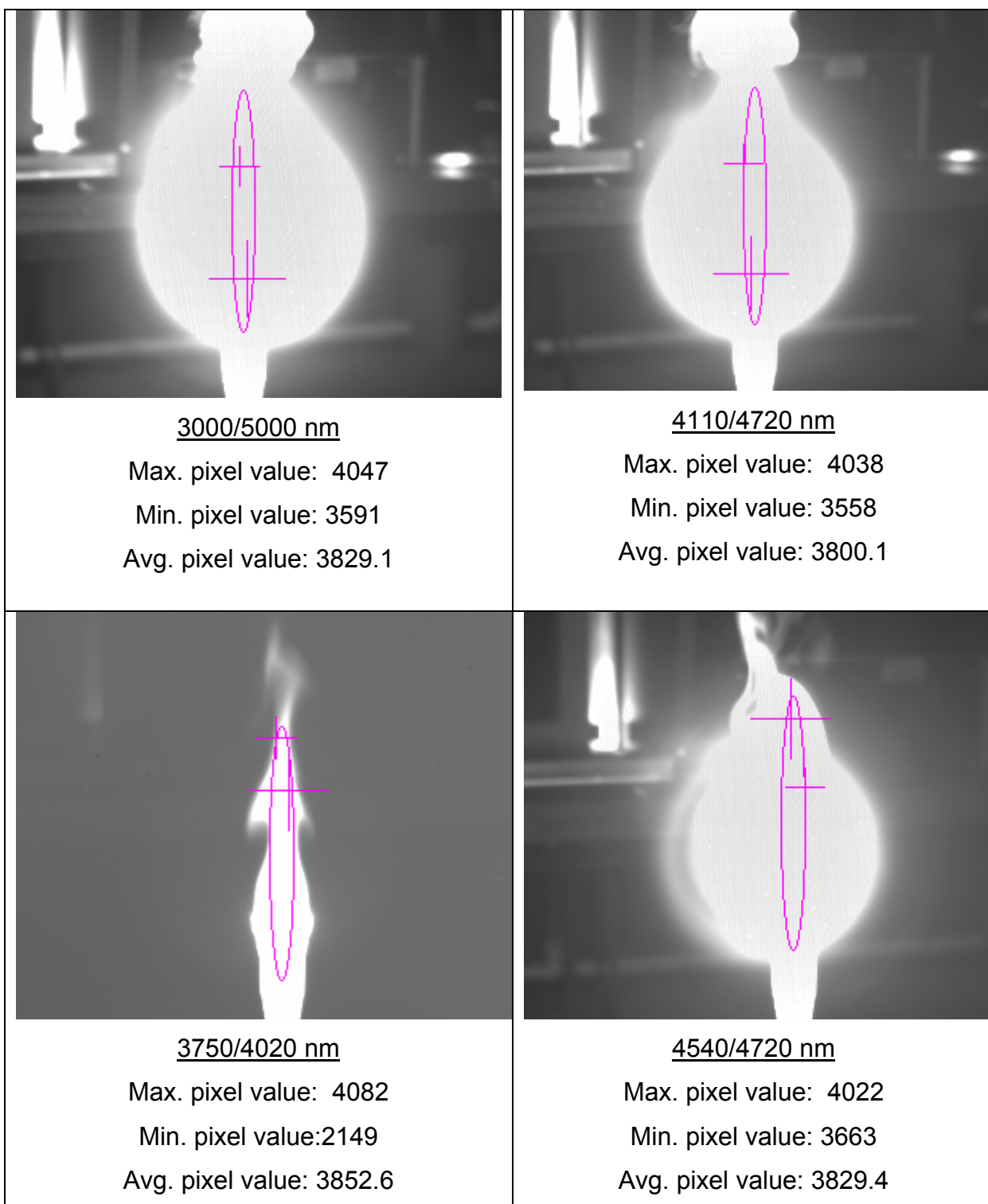


Figure 6.9 Image area statistics using the elliptical ROI.

(The large and small crosses correspond to maximum and minimum pixel values within the elliptical ROI, respectively.)

It is observed that all the images give similar maximum (large cross-hair) and minimum (small cross-hair) pixel intensity values. The same observation is made for the average pixel intensity for all the images. Besides, both the 3000/5000 nm and 4110/4720 nm filter bands have similar maximum and minimum positions. It is also observed in recorded video that the maximum position of the 3750/4020 filter band is fluctuating continuously. In other words, the maximum intensity seems to vary temporally. This is not observed for the other video clips. This observation is likely due to the fact that there is no dominant radiant energy source within this particular band. Conversely, the CO₂ emission peak dominates the thermal emission in the other three filter bands, hence resulting in consistently high radiant intensities and fixed maxima position. This conclusion further validates the possibility to use narrow band filter bands to identify the signature of hydrocarbon combustion. One may also use this anomaly to discriminate the target of interest with its background.

VII. CONCLUSIONS

Based on available laboratory equipment and settings, test methods were successfully developed to characterize thermal imagers in terms of SiTF, CTF, MTF and MRT. Specifically, both the existing Cincinnati and the newly purchased Merlin thermal imagers were characterized and compared. The Merlin camera is found to be superior in terms of resolution limit and contrast modulation. Besides, it has a wider dynamic range.

In the study of multi-narrow band imaging, three narrow bands within the 3 to 5 μm region were studied and analyzed with the intent to improve detection, identification and discrimination of fast moving air targets with plume and aerodynamic signatures. These selected narrow filters are the 3750/4020 nm, 4540/4720 nm and 4110/4720 nm bands. The first band is used to detect aerodynamic heating signature, the second band is used to detect the red spike in a plume signature while the last band is to isolate both the blue and red spikes of a plume signature. These filters were purchased and installed in the Merlin Camera. The performance characteristics of these individual narrow bands were then evaluated. The testing shows that their individual performances are poorer than without these narrow band filters when their CTF and MRT are compared. All the narrow band filters exhibit similar performance characteristics. It is concluded that the poor performance is largely due to the low radiant intensity transmitted through the narrow filters, resulting in low signal to noise ratio. In other words, the experiments are predominantly system noise limited. Hence, the study is inconclusive with respect to its imaging and detection performance characteristics. Finally, narrow band images of the propane flame from a Bunsen burner were acquired using the IRvista 2.51. These images were analyzed and compared and discussions were made specifically on their potential use in discriminating hydrocarbon emission. It is concluded that it is highly possible to correlate radiant intensity from various narrow bands to uniquely identify and

discriminate a target showing hydrocarbon combustion emission from other sources.

VIII. RECOMMENDATIONS FOR FUTURE WORK

There is significant potential for research in multi-narrow band imaging and further work has to be pursued to enhance its development.

Firstly, the performance characterization of narrow band filters will have to be revisited. There is a need to investigate and minimize existing system noise so as to truly reflect the performance of individual narrow band filters. Only then can conclusions be drawn in terms of their detection and imaging capability. This is important for the purpose of determining their effective operable range.

Secondly, it is worthwhile to acquire thermal images at a distance where the effect of atmospheric absorption is significant. With a hydrocarbon emission at longer range, this will effectively simulate an actual plume signature. This will confirm the use of various narrow band images to discriminate an actual plume emission. A final test could be to site this hydrocarbon emission against a background with different thermal sources to examine its effectiveness in discriminating the target of interest.

Last but not the least, there is a possibility to correlate these narrow band signatures with polarized signature as well as to fuse multiple narrow band images to further improve recognition and identification capabilities of thermal imagers.

THIS PAGE INTENTIONALLY LEFT BLANK

APPENDIX A

SPECIFICATION OF MERLIN InSb LABORATORY CAMERA (After http://www.indigosystems.com/product/merlin_specs.html dated 11 Oct 2004)

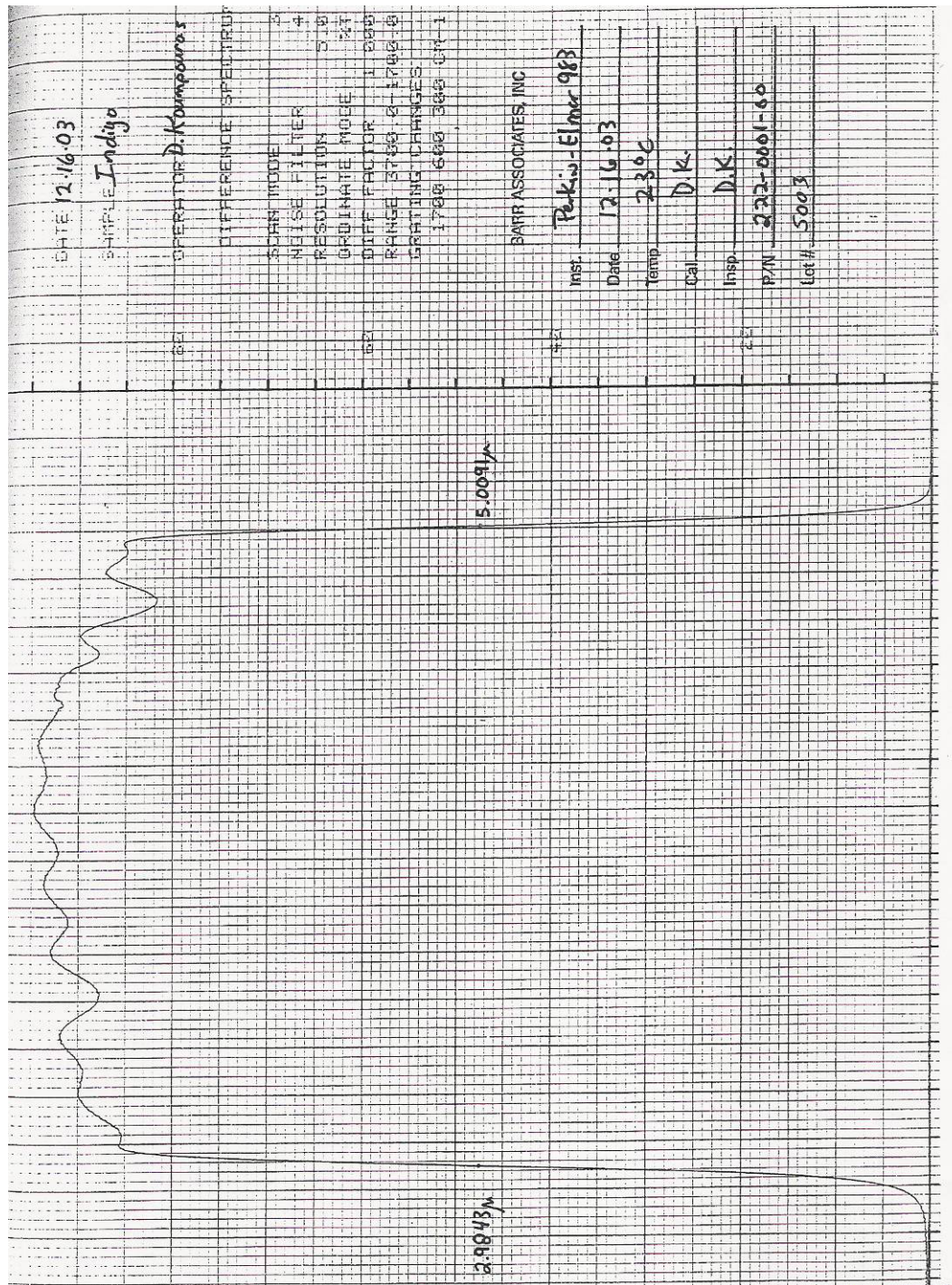
The following specification for the Merlin InSb Laboratory Camera was downloaded from the homepage of the Indigo Systems Corporation

	Merlin MID
Detector Type	InSb
Spectral Range	1 - 5.4 μm (3 - 5 μm set by cold filter)
Detector Size	30 x 30 μm
Array Format	320 x 256
Integration Time	5 μs - 16.5 ms
Camera f/#	2.3
Cooling Type	Integral Stirling or LN
NEdT [NEI]	< 25 mK (< 18 mK typical)
Analog Video	NTSC @ 30 Hz (PAL @ 25 Hz optional); S-Video
Digital Video	60, 30*, 15* Hz (50 Hz PAL), 12-bit corrected/uncorrected (*Reduced frame rate option disables analog video. This option not available for Merlin Uncooled.)
Remote Control	Button Panel & RS-232
Size	5.5 "H x 5.0 "W x 9.8 "L
Weight	9 lbs
Standard Temp Measurement	0 - 350 °C
Extended Temp Measurement	300 - 2,000 °C
Temp Accuracy	2 °C or 2%

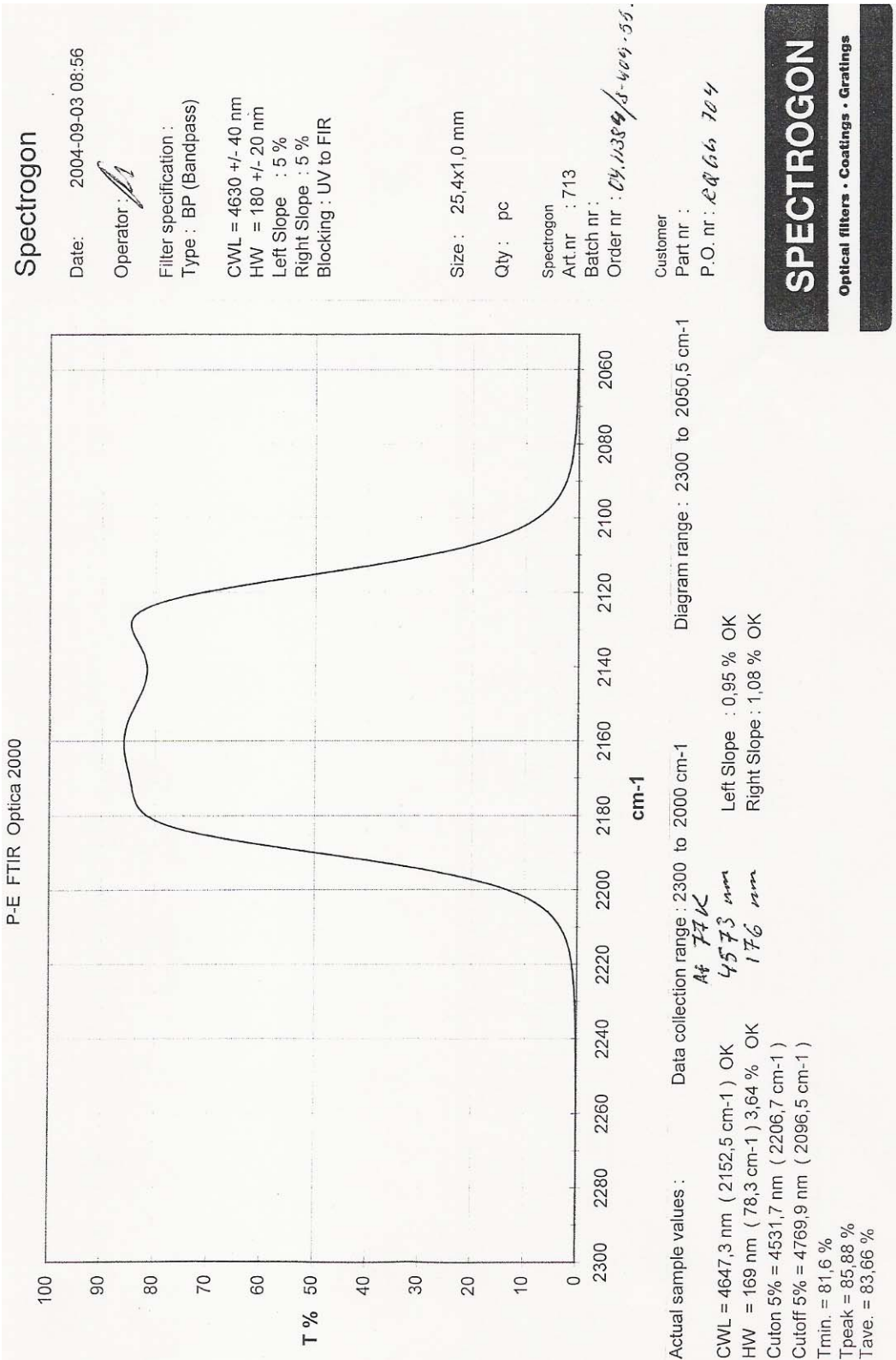
THIS PAGE INTENTIONALLY LEFT BLANK

APPENDIX B

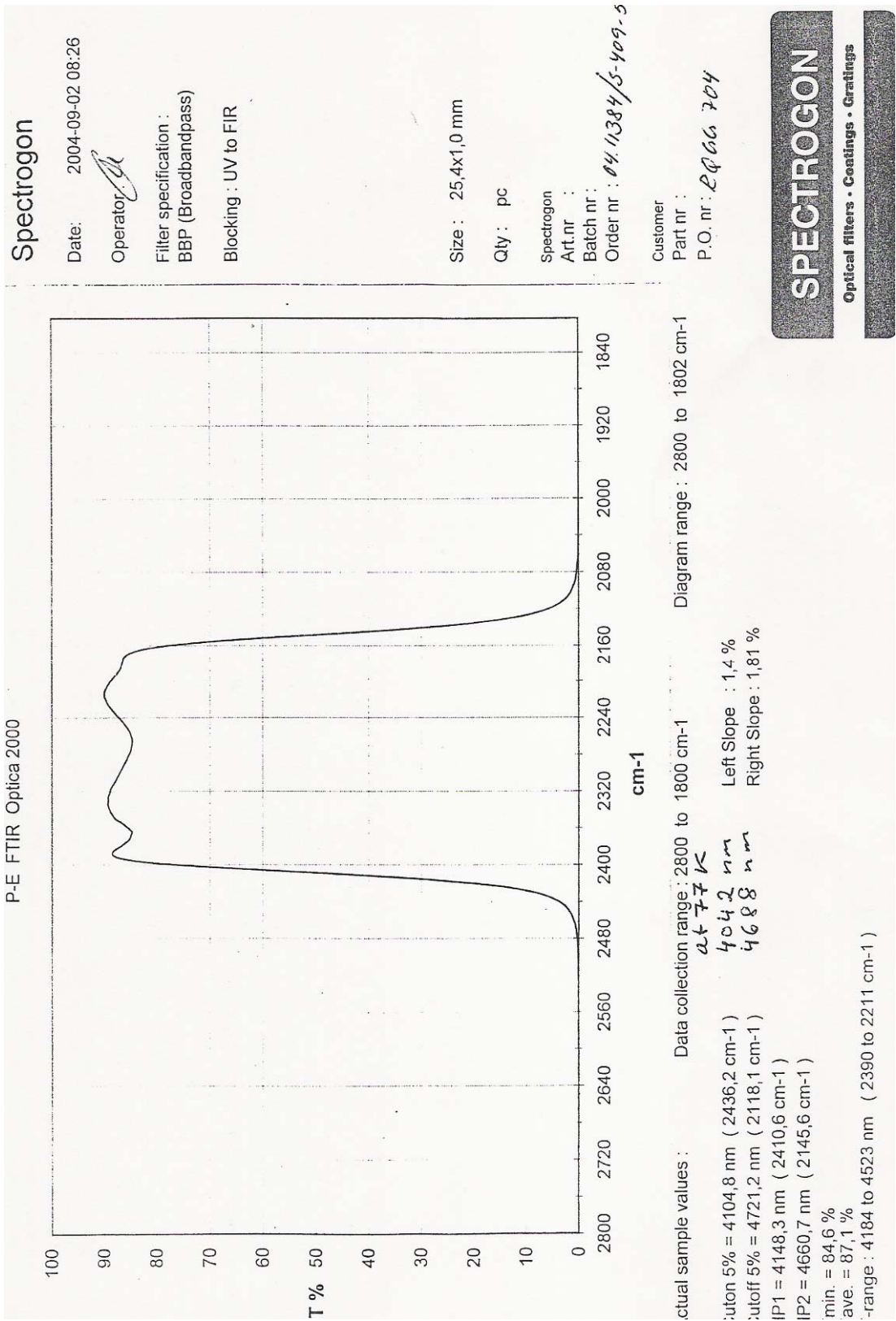
Filter Response of 3000/5000 nm filter



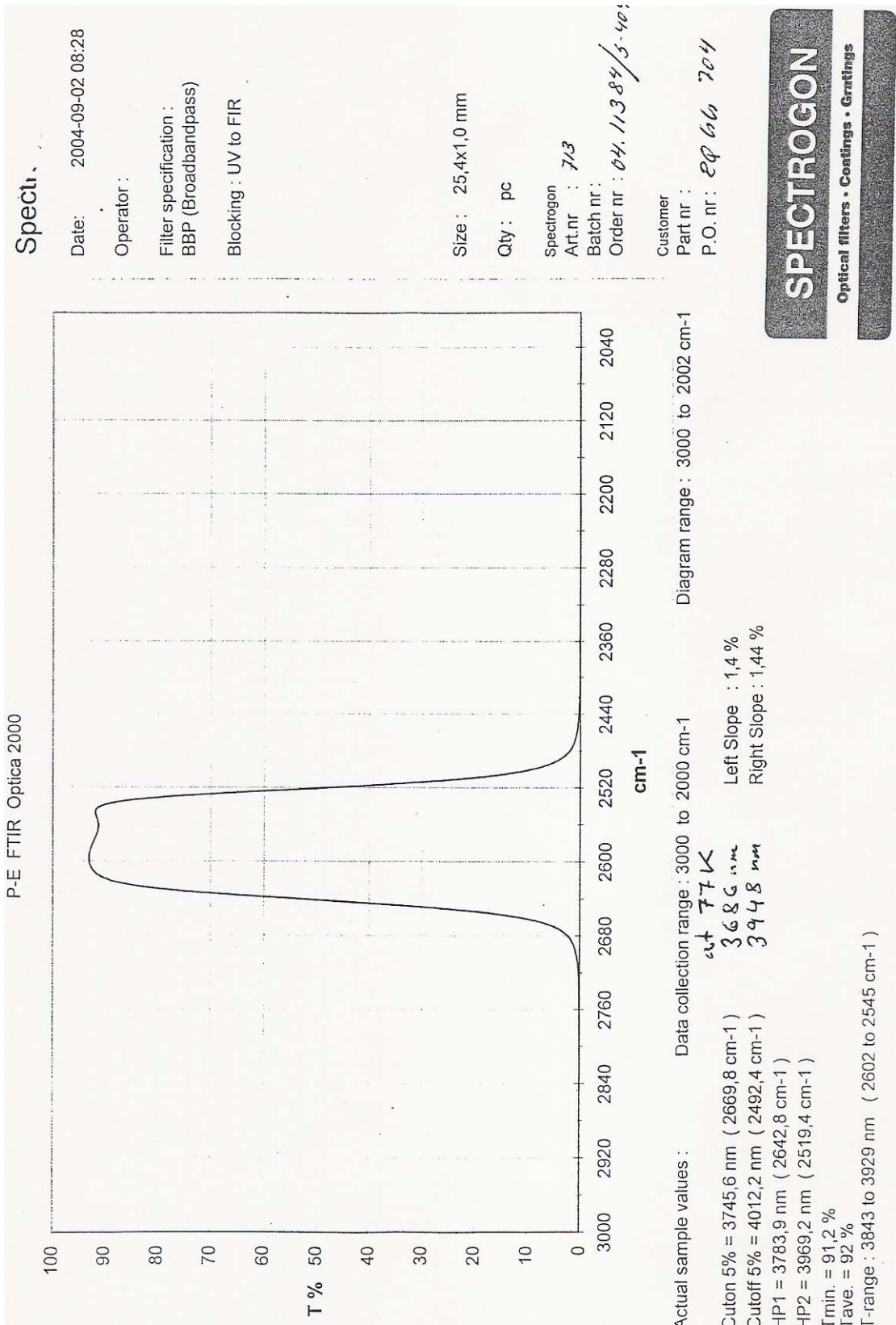
Filter Response of 4540/4720 nm filter



Filter Response of 4110/4720 nm filter



Filter Response of 3750/4020 nm filter



APPENDIX C

The Operation of Image Intensity Windowing Statistical Tool [18]

The intensity histogram is found in the lower right corner of the application window as shown in Figure C1. The left top image shows the live video or still image acquired.

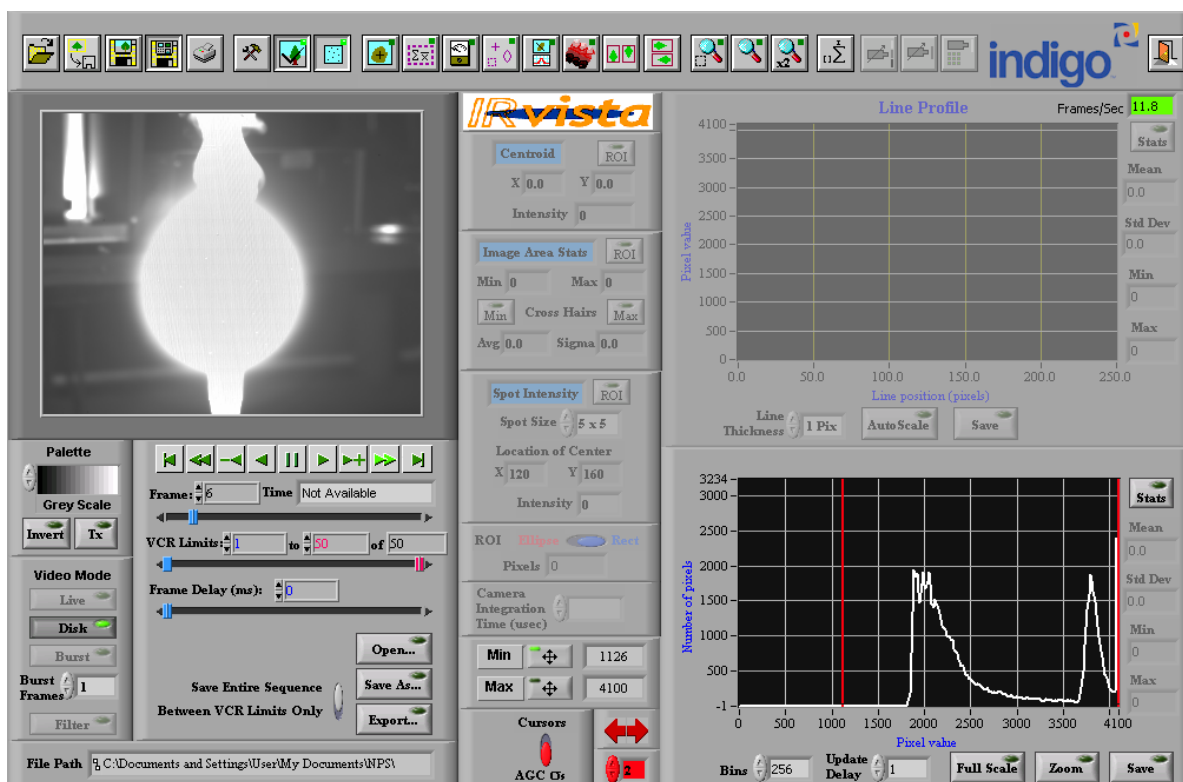


Figure C1 IRvista application window

Image compression controls are located to the left of the histogram and below the histogram (Figure C2). It is often useful to apply a data compression routine to the image as follows:

For a 12 bit image with $0 < I < 4096$,

A pixel with intensity below I_{\min} is replaced by 0.

A pixel with intensity above I_{\max} is replaced with 255.

A pixel with intensity $I_{\min} < I < I_{\max}$ is replaced by

$$I = (I - I_{\min}) * 255 / (I_{\max} - I_{\min})$$

This data compression algorithm can enhance small differences in pixel intensity that would otherwise not be obvious and is sometimes called intensity windowing.

I_{\max} and I_{\min} can be selected from the histogram controls. The histogram, a graph of the number of pixels with intensity I versus I , features two cursors. The lower cursor gives the value of I_{\min} and the upper cursor gives the value of I_{\max} . These cursors can operate in either of two modes.

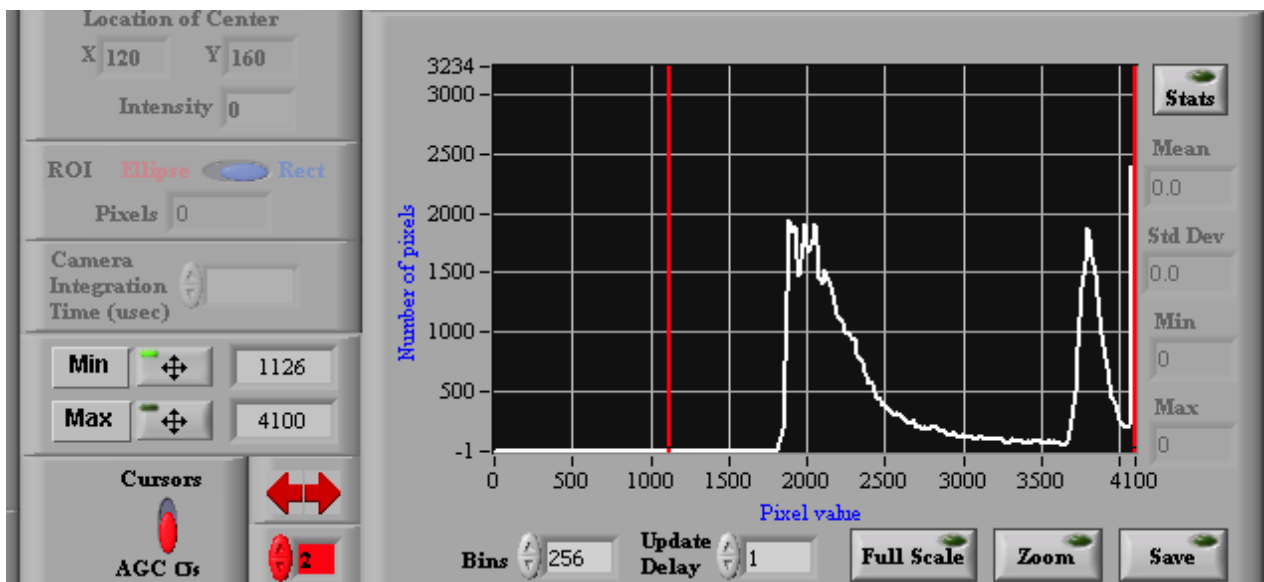


Figure C2 Image Intensity Windowing controls

If Automatic Gain Control (AGC) is turned on, then the mean and standard deviation of the histogram are measured and the cursors (and thus the intensity limits) are set depending on the n value. 'n' is set by the selector to the right of the cursory/AGC switch. The cursor can be adjusted when the cursors/AGC selector is switched to cursor.

The number of bins in the histogram is normally set to 256. With a 12-bit image there are 4096 possible values of intensity, and thus each bin in the histogram contains the number of pixels with 16 different intensity values. The number of bins can be adjusted. Setting the number of bins larger than 256 slows acquisition and also results in larger statistical fluctuations in histogram values.

The stats button on the right side of histogram allows the mean, standard deviation, min and max of the intensity histogram to display.

Note that the image compression is normally set to on, but it can be turned off from the menu. Besides, all images saved to disk are saved in raw form. The data saved on disk is not intensity windowed, but the recalled data will be intensity windowed for display in disk mode. This allows the user to view the saved image stream with different windowing settings and assures that no information is lost when the data is saved to disk.

THIS PAGE INTENTIONALLY LEFT BLANK

LIST OF REFERENCES

1. J. M. Lloyd, "Thermal Imaging Systems", Plenum Press, New York, 3rd Printing, 1982.
2. Gerald C. Holst, "Infrared Imaging Systems Testing", The Infrared & Electro-Optical Systems Handbook, Vol. 4, Chapter 4, 1996.
3. Mustafa Celik, "Measurements and Modeling Enhancements for the NPS Minimum Resolvable Temperature Difference Model, VISMODII" Master of Science in System Engineering, Naval Postgraduate School, Sep 2001.
4. G.W. Edwards, "Objective Measurement of Minimum Resolvable Temperature Difference (MRTD) for Thermal Imagers," SPIE Proceedings on Image Assessment: Infrared and Visible, Vol. 467, pp.47-54, 1983
5. Ron J. Pieper, Alfred W. Cooper, Mustafa Celik and Yucel Kenter, "Objective MRTD Experimental Measurements Compared with Predictions Based on the Visibility Model", Proceedings of the SPIE, Volume 5076, pp. 196-207 (2003).
6. Tung, Yan Foo, "Testing and Performance Characterization of the Split-field Polarimeter in the 3-5 μm waveband", Master Thesis, Naval Postgraduate School, Dec 2003.
7. Northrop Grumman Electronic Systems, "Dual Spectrum Polarization/Multi-spectral Seeker for Boost Phase Intercept" dated Jan 2003.
8. D. Farson, R. Richardson and X. Li, "Infrared Measurement of Base Metal Temperature in Gas Tungsten Arc Welding", Department of Industrial, Welding and Systems Engineering, The Ohio State University.
9. Gerald C. Holst, Electro-optical Imaging System Performance, JCD Publishing and SPIE Optical Engineering Press, 2000.
10. <http://www.profc.udec.cl/~gabriel/tutoriales/rsnote/cp1/1-4-1.gif>, dated 5th Aug 2004.
11. <http://www.profc.udec.cl/~gabriel/tutoriales/rsnote/cp1/1-7-1.gif>, dated Aug 2004.
12. J. M. Lloyd, "Chapter 1: Fundamentals of Electro-Optical Imaging Systems Analysis", The Infrared & Electro-Optical Systems Handbook, Vol.4, SPIE Optical Engineering Press, 1996.

13. David. L. Shumaker, James. T. Wood and Clinton R. Thacker, Infrared Imaging Systems Analysis.” ERIM Series in Infrared & Electro-optics, 1988.
14. Merlin InSb Laboratory Camera User’s Guide Version 120 414-0010-10, Indigo Systems Corporation.
15. K. C. Hepfer, MRT and MDT Functions, Naval Surface Weapons Center Program Description, 1982
16. Joseph S. Accetta, “Chapter 4: Fundamentals of Electro-Optical Imaging Systems Analysis”, The Infrared & Electro-Optical Systems Handbook, Vol.5, SPIE Optical Engineering Press, 1996.
17. Anthony J. LaRocca, “Artificial Sources”, The Infrared & Electro-Optical Systems Handbook, Vol. 1, Chapter 2, 1996.
18. IRvista 2.51 User’s Manual 321-0028-10, Indigo Systems Corporation.
19. Richard D. Hudson, JR., “Infrared System Engineering”, John Wiley & Sons, Inc. 1969.
20. Edson F.C. Guimaraes, “Investigation of Minimum Resolvable Temperature Difference Formulation for Polarized Thermal Imaging Range Prediction”, Master Thesis, Naval Postgraduate School, Sep 1999.
21. Y.Ikeda, T.Kurahashi, N. Kawahara and E. Tomita, “Temperature Measurement of Laminar Propane/Air Premixed Flame Using Detailed OH Spectra Intensity Ratio” Department of Mechanical Engineering, Okayama University.
22. David J. McCaa, “Spectral Radiance Measurements of Exhaust Plumes from Scale Model Rocket Engines” Applied Optics, Vol. 7, No. 5, Pg 899, 1968.

INITIAL DISTRIBUTION LIST

1. Defense Technical Information Center
Ft. Belvoir, Virginia
2. Dudley Knox Library
Naval Postgraduate School
Monterey, California
3. Department Chairman, Code PH
Department of Physics
Naval Postgraduate School
Monterey, California
4. Professor A.W. Cooper, Code PH/Cr
Department of Physics
Naval Postgraduate School
Monterey, California
5. Professor Gamani Karunasiri, Code PH/Kg
Department of Physics
Naval Postgraduate School
Monterey, California
6. Director, Temasek Defence Systems Institute
Professor Yeo Tat Soon
Singapore
7. Singapore Armed Forces
Quek, Yew Sing
Singapore